JOURNAL OF MATERIALS SCIENCE 27 (1992) 4261–4281

Review
Influence of some alloying elements on decomposition of a Co–3 wt% Ti alloy

J. SINGH*
GE Aircraft Engine, 1 Neumann Way, Cincinnati, OH 45215, USA

C. SURYANARAYANA
Institute for Materials and Advanced Processes, University of Idaho, Moscow, ID 83843-4195, USA

The effect of minor alloying additions (La, Fe and Nb) on the decomposition behaviour of a Co–3 wt% Ti alloy is discussed. Optical microscopy coupled with electron microscopy and diffraction have aided in elucidating the microstructural evolution in these alloys. The solid solutions of binary and ternary alloys decomposed on ageing by the spinodal mode. The different stages of coarsening of the precipitates are discussed, as are kinetics and morphological changes during precipitation of binary and ternary alloys. After long ageing times, discontinuous precipitation set in. The discontinuous product is close to equilibrium and is considered to be driven by the difference between coherent and incoherent equilibria in these systems. Coherent precipitation occurred by volume diffusion whereas incoherent precipitation reactions were determined by grain-boundary diffusion. The microstructural evolution has been correlated with the observed variation in hardness and yield strength at different stages of decomposition.

Nomenclature

T_s	Critical temperature for coherent spinodal decomposition
λ	Wavelength of modulations
K	Rate constant
γ	Interfacial energy
ρ	Density of alloy
W	Weight fraction
M	Atomic weight
V_m	Molar volume of Co_3Ti
a	Lattice parameter of matrix
N	Avogadro's number
a_p	Lattice parameter of precipiate
Δa	Mismatch lattice parameter
S	Size of precipitate for loss of coherency
V_v	Volume fraction of precipitate
t	Foil thickness
$V_{v'}$	Apparent volume fraction
D	Measured precipitate size
C_e	Solvus composition
A	Constant
B	Constant
A	Amplitude of modulation
n	Distortion parameter
Y	Young's modulus
$\boldsymbol{b}$	Burgers vector
β	Wave vector
σ_c	Critical resolved shear stress
Z	Spacing of misfit dislocations
a_{ss}	Lattice parameter of solid solution
C	Concentration in atomic fraction
b_0	Constant
b_1	Constant
b_2	Constant
YS	Yield strength
D_b	Grain-boundary diffusivity
D_v	Volume diffusivity
p^{chem}	Chemical driving force
X_0	Composition of supersaturated alloy
X_e	Equilibrium concentration
V	Growth velocity
b	Interatomic distance
f	Fraction of driving force
ΔG	Gibb's free energy
n	Misfit parameter
F	Traction force
r_0	Radius of lamellar rods
N	Number of rods per unit area
G	Growth of discontinuous precipitation (cell)
X_m	Matrix composition ahead of interface
X_β	Composition of second phase (Co_3Ti)
Q	Activation energy
Γ	Effective thickness of boundary

1. Introduction

The ever increasing demand for the development of

* Present address: Department of Materials Science and Engineering, North Carolina State University, Rayleigh, NC 27695-7907, USA.

0022–2461

cobalt-based superalloys relies generally on solid solution strengthening and carbide strengthening concepts [1, 2]. However, because nickel-base superalloys owe their attractive strength properties to the precipitation of $\gamma(Ni_3Al)$, an intermetallic compound [3], there is a strong incentive to achieve similar results in cobalt-based alloys. Using this mode, and a candidate material based on precipitation of Co_3Ti, it was felt that the precipitation of Co_3Ti by spinodal transformation will lead to enhanced strength. Most of the earlier work had been carried out on concentrated Co–Ti alloys and resulted in correlation of mechanical properties with the developed microstructures [4–16]. There was thus scope for a detailed study of dilute alloys. Hence a dilute Co–3 wt % Ti binary alloy was chosen. The influence of small quantities of lanthanum, niobium and iron on the microstructure and mechanical properties of the Co–3 wt % Ti alloy are discussed.

2. Experimental procedure

The compositions of the binary and ternary alloys investigated are presented in Table I. They were supplied in the form of rods of 20 mm diameter and 150 mm length. In order to have the required dimensions for mechanical testing and microstructural observations, the alloys were hot forged with intermediate heating in an oil furnace followed by cold rolling.

Samples were solution treated in evacuated silica tubes at 1473 K for 1 h and then quenched in water and aged at temperatures ranging between 823 and 1073 K. For optical metallography, 5% Nital was used as an etchant. Thin foils were prepared using a twin jet electropolisher with a solution of 10% perchloric acid in methanol at 258 K. The foils were examined in either a Philips EM430 transmission electron microscope (TEM) or a Vacuum Generator HB-5 scanning transmission electron microscope (STEM).

3. Results and discussion

Microstructural evolution in the binary and ternary alloys can take place in one or more of the following three modes:

1. homogeneous decomposition/transformation by homogeneous nucleation and growth, i.e. spinodal decomposition;
2. heterogeneous/grain-boundary precipitation, i.e. discontinuous precipitation;
3. transgranular decomposition by heterogeneous nucleation and growth.

3.1. Microstructural observation

Direct microstructural examination provides much useful knowledge about spinodal decomposition. Optical microscopy can be used only after considerable coarsening of the precipitates has occurred and therefore has been of limited use. Electron microscopy offers a powerful method for observing the early stages

TABLE I Compositions of the alloys

Alloy	wt %
1	Co–3% Ti
2	Co–3% Ti–0.1% La
3	Co–3% Ti–1% Nb
4	Co–3% Ti–2% Nb
5	Co–3% Ti–1% Fe
6	Co–3% Ti–2% Fe

of spinodal decomposition in alloys. Before discussing further the general ways of establishing spinodal decomposition in the alloys, it would be useful here to show the microstructural evolution of the aged alloys. Figs. 1–4 show the general microstructural evolution in the binary and ternary alloys aged at 873–973 K for up to 20 days. Because the microstructural features appear to be similar in the binary and ternary alloys, the electron micrographs from the ternary Co–3% Ti–2% Nb alloy aged at 873 K in Fig. 4 would be taken as typical examples for a general discussion. Fig. 4a represents the microstructure of the as-quenched alloy showing a high density of stacking faults in the f c c matrix. The microstructure does not give any evidence of decomposition during quenching. Fig. 4b shows the modulated structure after ageing at 873 K for 5 min. The modulation was found to be along $\langle 1\,0\,0 \rangle$ directions. On ageing for a longer period (48 h), a breakdown of the modulations takes place with the formation of distinct cuboidal precipitates aligned in rows (Fig. 4c). In addition, some allotriomorphs are observed at the grain boundaries, as indicated by arrows. The density and spacing between the allotriomorphs is found to increase with ageing time. Coarsening of cuboidal precipitates is observed on ageing for longer periods (Fig. 4d and e); the precipitates are still coherent with the matrix. The coarsening of modulations, breakdown of modulations into cuboids, and coarsening of cuboids are all found to occur along $\langle 1\,0\,0 \rangle$ directions. At later stages of ageing, discontinuous precipitation is observed only at high-angle grain boundaries (Fig. 4f).

The main differences in the microstructures of the binary and ternary alloys are the initial kinetics of decomposition, coarsening of cuboid precipitates and growth rate of discontinuous precipitation. In all the alloys, the cuboid precipitates are identified as the ordered Co_3Ti phase. In addition, at later stages of coarsening, the cuboid precipitates lose coherency with the matrix, and interfacial dislocations and Moiré fringes are observed (Fig. 5).

On ageing the binary and ternary alloys above their spinodal decomposition temperature limit, precipitation at grain boundaries is observed (Fig. 6). This type of precipitation falls into the third category, i.e. transgranular precipitation by heterogeneous nucleation and growth.

The mechanism of spinodal decomposition in a given alloy can be established by the following methods.

(i) The microstructural sequence method suggested by Laughlin and Cahn [17] depends on a study of

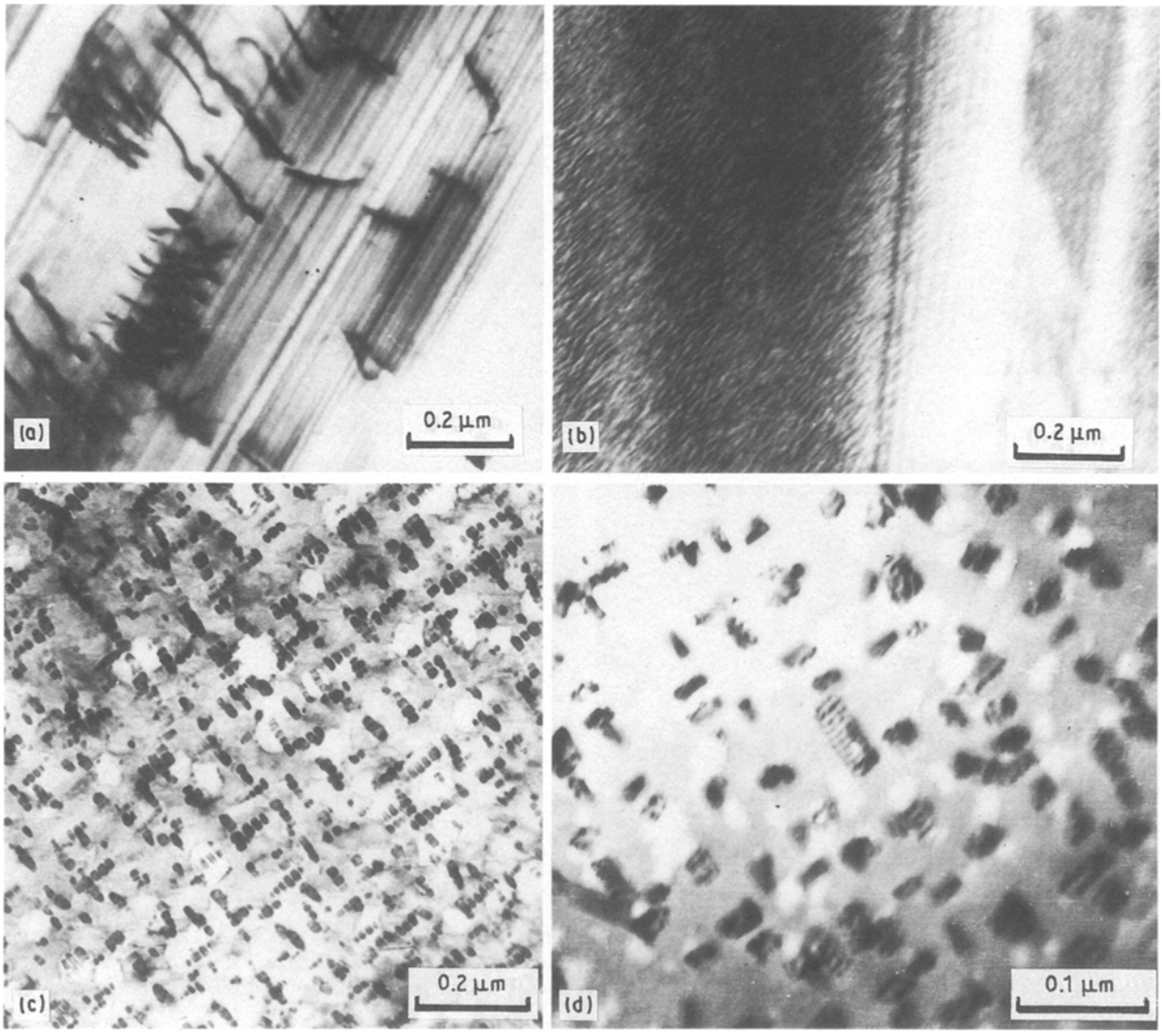

Figure 1 Transmission electron micrographs of Co–3% Ti alloy (a) as-quenched, showing high density of stacking faults; (b) aged at 923 K for 1 h, showing modulations; (c) aged at 923 K for 48 h, showing discrete cuboidal precipitates; (d) aged at 973 K for 360 h, showing Moiré fringes.

variation of the modulation contrast which depends on the amplitude of the concentration fluctuations (i.e. there will not be any change in the wavelength of modulations). This method is very sensitive to the polishing conditions, and thickness and orientation of the foils. Further, it is not always possible to use this method in those alloys which contain considerable stacking faults in the quenched condition (e.g. cobalt-based alloys).

(ii) The early stage of spinodal decomposition can be established by electron diffraction analysis. In the electron diffraction patterns, one pair of satellites appears for $\{h\,0\,0\}$ reflections, two pairs for $(h\,k\,0\}$ reflections, and three pairs for $\{h\,k\,l\}$ reflections. The satellite reflections (or side bands in X-ray diffraction patterns) could be explained by a periodic composition modulation in $\langle 1\,0\,0\rangle$ directions. The separation of the side bands is the largest for $\{h\,0\,0\}$ reflection and least for $\{h\,h\,h\}$ reflections [18, 19].

(iii) The initial precipitation by a spinodal decomposition mode can be established by considering the temperature dependence of the growth of modulation [19, 20]. The temperature dependence of the growth mode for modulation for the Co–3% Ti–2% Nb alloy is presented in Fig. 7. In this case, at an early stage of ageing at temperature T, the wavelength of the modulations, λ, should be inversely proportional to the square root of the temperature difference $(T_s^* - T)$, where T_s^* is the critical temperature for coherent spinodal decomposition (1023 K for this alloy). Thus, the plot of log λ versus log $(T_s^* - T)$ will give linear relationship with slope $-1/2$ (Fig. 8).

Both points (ii) and (iii) unambiguously establish that the Co–3% Ti–2% Nb alloy decomposes by a spinodal mode.

The T_s^* temperature can be determined experimentally as follows. The Co–3% Ti–2% Nb ternary alloy shows modulations and cuboid precipitation on ageing up to 973 K (Fig. 4) but shows general precipitation on ageing above 1073 K (Fig. 6c and d). Therefore, T_s^* can be assumed to be 1023 K, half-way between 973 and 1073 K. The T_s^* temperature for the other binary and ternary alloys could be also determined in a similar manner.

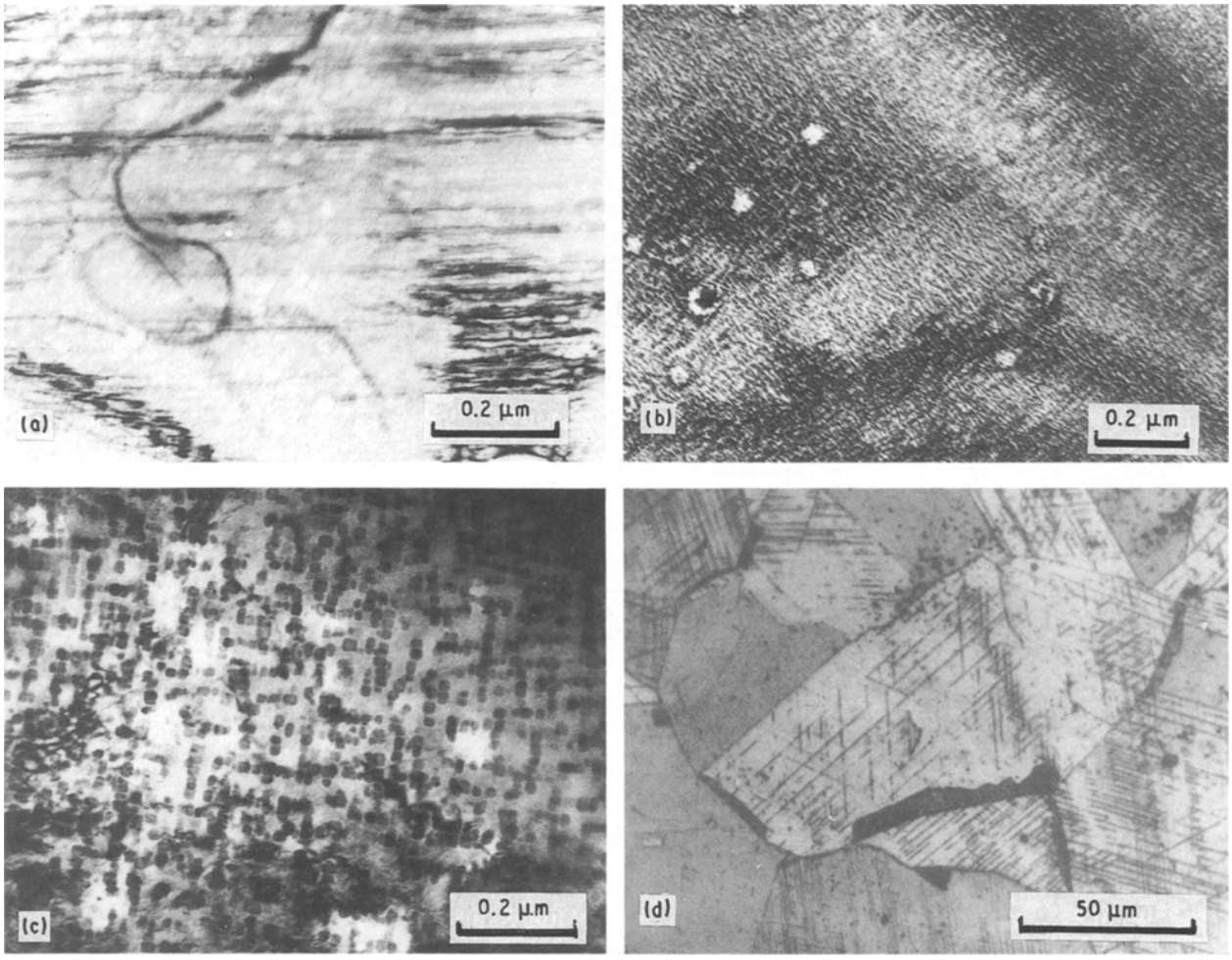

Figure 2 Transmission electron micrographs of Co–3% Ti–0.1% La alloy aged at 823 K: (a) as-quenched, showing slight evidence of decomposition; (b) for 12 h, showing modulations; (c) for 96 h, showing the coarsening of cuboidal precipitates; (d) for 480 h, optical micrograph showing discontinuous precipitation at the grain boundaries. Note the line markings due to the fcc to hcp allotropic transformation.

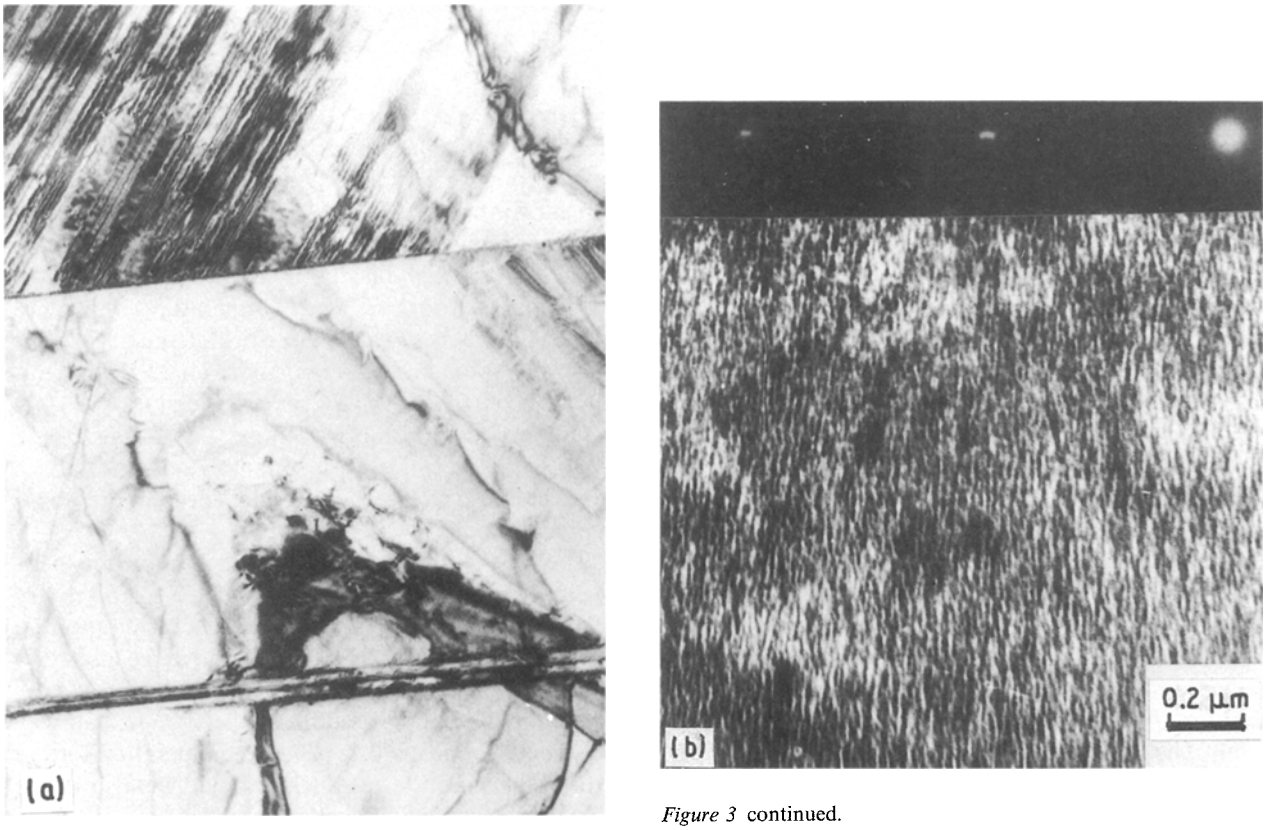

Figure 3 continued.

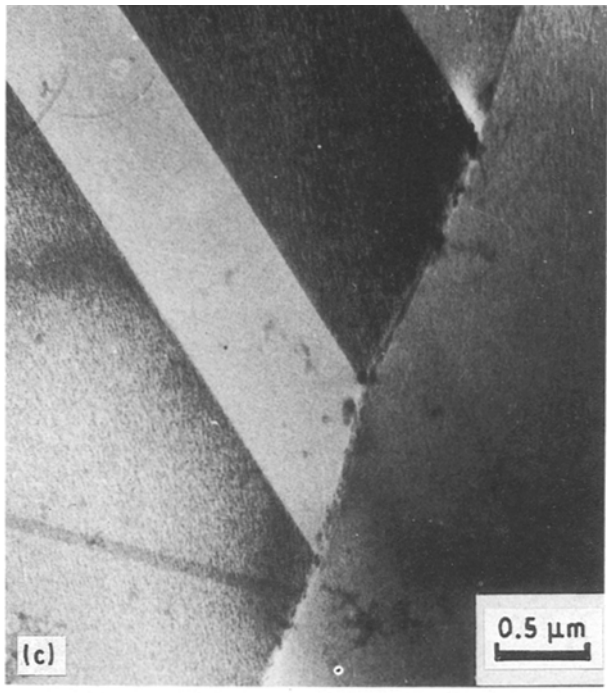

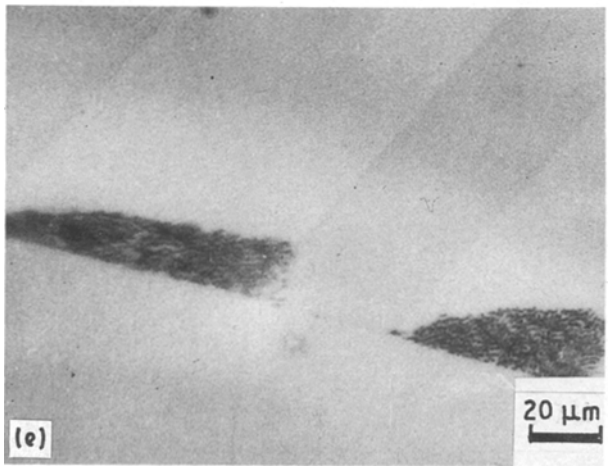

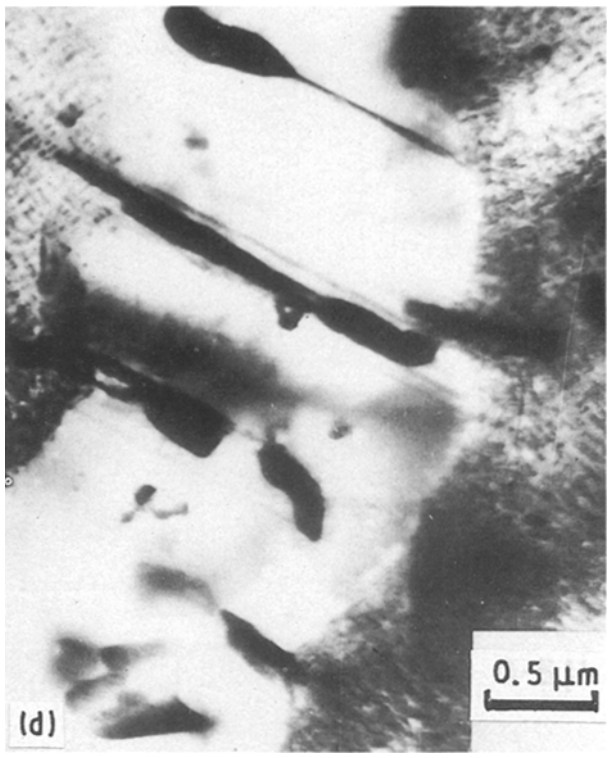

Figure 3 Transmission electron micrographs of Co–3% Ti–2% Fe alloy aged at 873 K: (a) as-quenched, showing stacking faults; (b) for 1 h: dark field using 200 matrix reflection and selected area diffraction (SAD) pattern (inset) showing satellites around 200: (c) for 15 min, showing modulated structure uneffected by twin boundary; (d) for 48 h, showing coherent cuboidal precipitates with denuded grain-boundary region; (e) 823 K for 384 h, showing discontinuous precipitation.

3.1.1. Coarsening behaviour

On the basis of above microstructural observations, the precipitation sequence in these alloys can be proposed as: as-quenched structure → formation of modulations → coarsening of modulations → breakdown of modulations into cuboids → coarsening of cuboids → coherency loss of cuboids → discontinuous precipitation or coarsening. These different stages of coarsening are discussed in the following sections.

3.1.1.1. Stage I: coarsening. In all the alloys studied, spinodal decomposition was followed by a coarsening of the modulated microstructure resulting in an increase in wavelength with ageing time. This corresponds to Stage I of spinodally decomposed alloys. The cube of the wavelength directly measured from the micrographs has been plotted as a function of time (Fig. 9).

The activation energy for the coarsening of the modulations can be calculated by plotting ln (KT/C) versus $(1/T)$ where K is the rate constant. Activation energies of 320, 340, 319, and 331 kJ mol^{-1}, respectively, for the binary Co–3% Ti, Co–3% Ti–0.1% La, Co–3% Ti–2% Fe, and Co–3% Ti–2% Nb alloys are obtained. The activation energy evaluated for the binary alloy is comparable to that for volume diffusion of titanium in cobalt, namely 281 ± 19 kJ mol^{-1} [21]. It is thus concluded that volume diffusion is the operating mechanism for coarsening of the modulations in Stage I. A similar comparison of results for the ternary alloys is not possible because diffusion data for these alloys is not available.

3.1.1.2. Stage II: evolution. A breakdown of the modulated microstructure occurs during this stage, yielding discrete cuboidal particles. For the present series of alloys, the onset of breakdown of the modulations takes place when the wavelength is about 20 nm. Further, after the initial breakdown, the cuboidal particles are arranged into rafts with a regular periodicity. The spacing of the particles is comparable to the modulation wavelength before breakdown, while the size of the cuboids is about 10 nm. This stage of microstructural evolution in these alloys corresponds to the peak hardness (to be discussed later).

3.1.1.3. Stage III: coarsening. Coarsening of discrete cuboidal precipitate particles occurs according to the Lifshitz–Slyozov–Wagner (LSW) [22, 23] mechanism

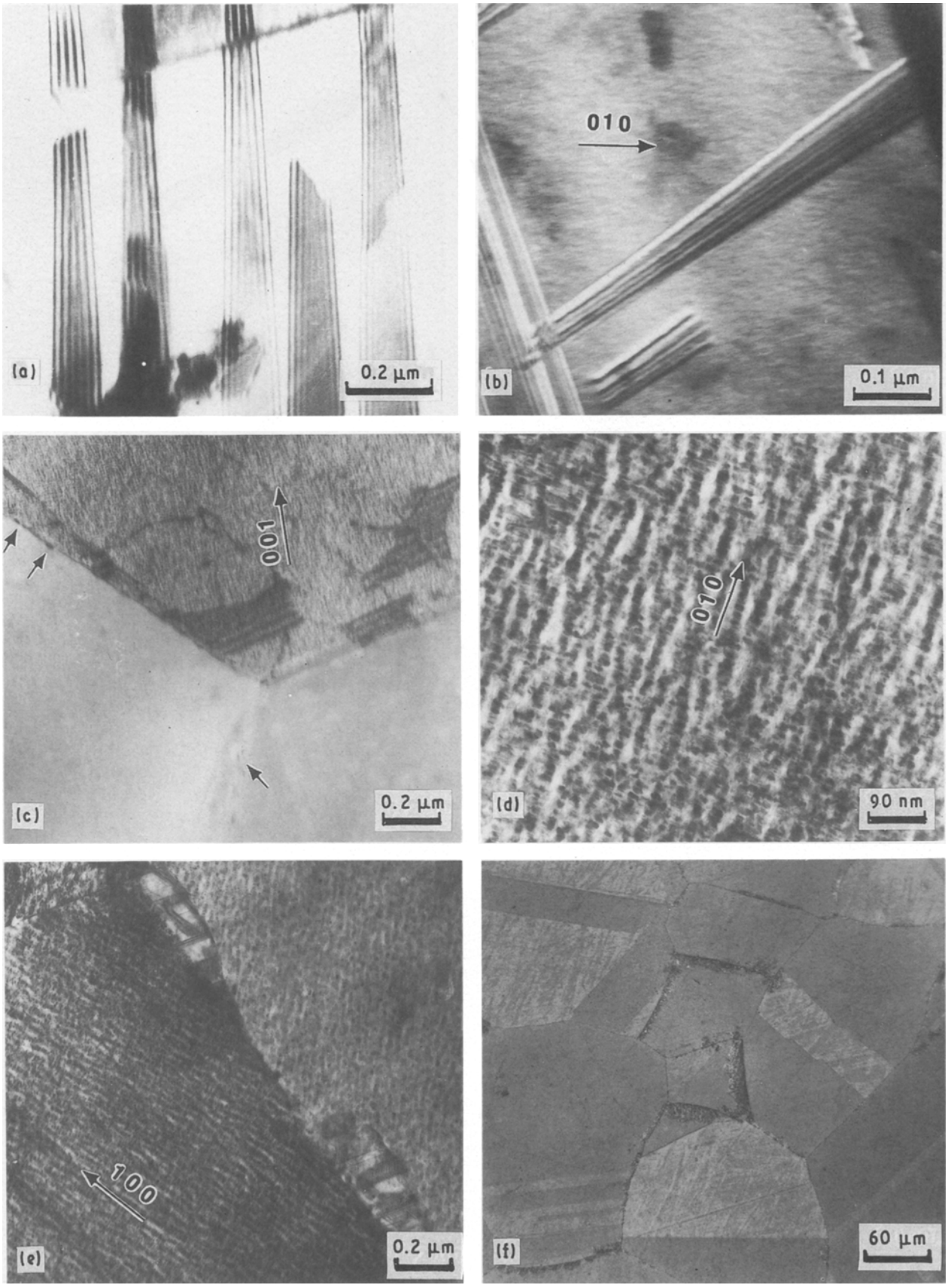

Figure 4 Transmission electron micrographs of Co–3% Ti–2% Nb alloy aged at 873 K: (a) as-quenched showing stacking faults; (b) for 5 min, showing modulations; (c) for 48 h, showing coarsening of modulations and few allotriomorphs at the grain boundaries; (d) for 360 h, showing homogeneously distributed coherent cuboidal precipitates along the $\langle 0\,1\,0 \rangle$ direction; (e) growth of discontinuous cells at the grain boundary; (f) for 480 h, optical micrograph showing discontinuous precipitation at grain boundaries.

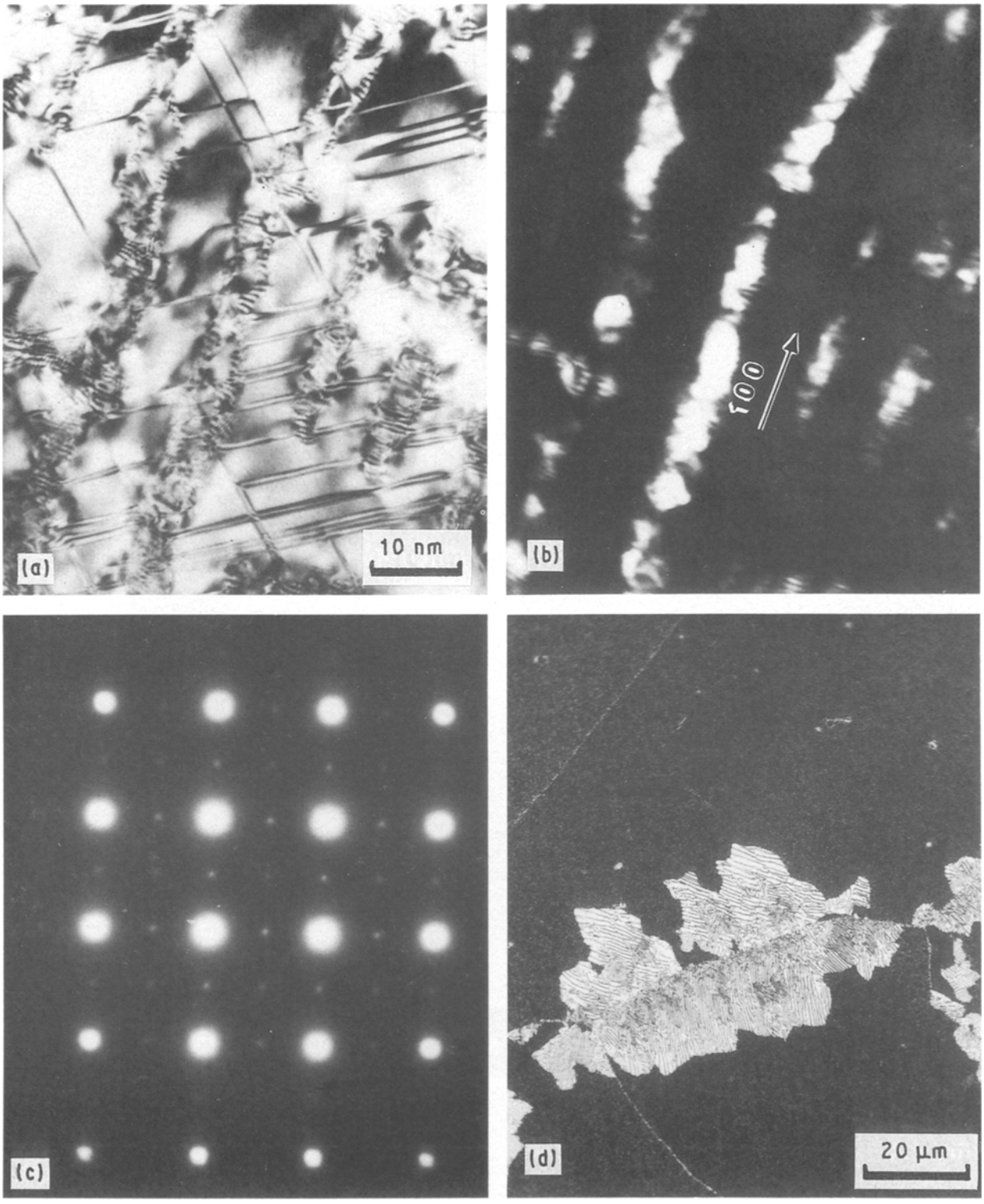

Figure 5 Transmission electron micrographs of Co–3% Ti–2% Nb alloy aged at 973 K for 48 h: (a–c) bright-field, dark-field and corresponding SAD pattern showing the loss of coherency and coalescence of cuboids along ⟨1 0 0⟩ directions; (d) aged at 973 K for 60 h, optical micrograph showing discontinuous precipitation.

during this stage. Initially, the particles tend to have nearly equal sizes ($\approx$ 10 nm) and uniform spacing ($\approx$ 20 nm). However, as coarsening proceeds, rows of particles are formed in such a way that the inter-particle spacing ($\approx$ 5 nm) within the rows is rather small but the inter-row gap ($\approx$ 35 nm) is much larger (Fig. 4d). These rows are parallel as well as perpendicular to each other. In the case of isolated rows, the central particle is the largest in size and further, the particle section is rectangular with the larger dimension being perpendicular to the row (Fig. 1c).

The interfacial energy, γ, of ⟨1 0 0⟩ faces of Co_3Ti cuboids in the binary Co–3% Ti alloys was estimated using the relationship [24]

$$\gamma = 9KRT/8DCV_m^2 \quad (1)$$

The diffusion coefficient, D, of the solute in the matrix during precipitate coarsening was evaluated to be

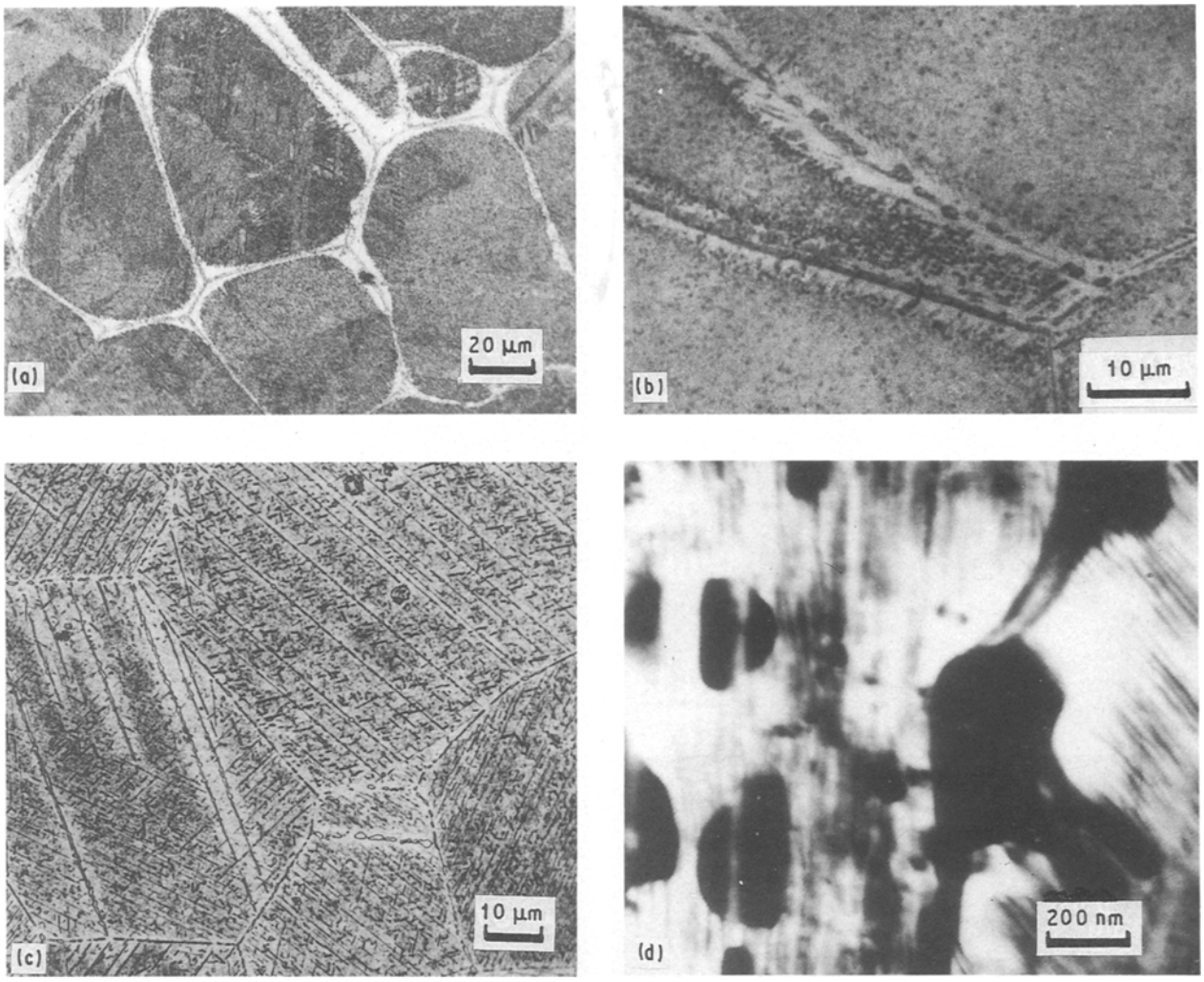

Figure 6 Optical micrographs of the binary and ternary alloys showing general precipitation and grain-boundary precipitation. (a) Co–3% Ti alloy aged 973 K for 170 h. (b) Co–3% Ti–2% Fe alloy aged at 923 K for 192 h. (c) Co–3% Ti–2% Nb alloy aged at 1073 K for 360 h. (d) Transmission electron micrograph of (c) aged at 1073 K for 24 h showing incoherent matrix and grain-boundary precipitations.

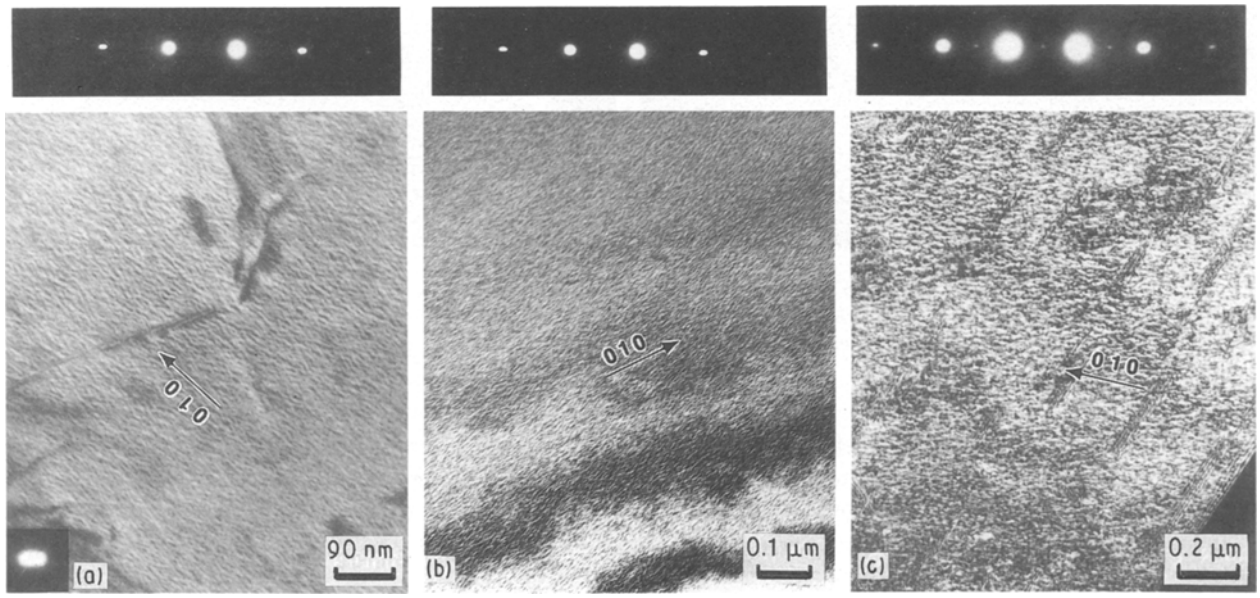

Figure 7 Transmission electron micrographs of Co–3% Ti–2% Nb alloy aged at different temperatures for 15 min, and corresponding diffraction patterns indicating the difference in satellite separation in accordance with the difference in wavelength: (a) 873 K, (b) 923 K, (c) 973 K.

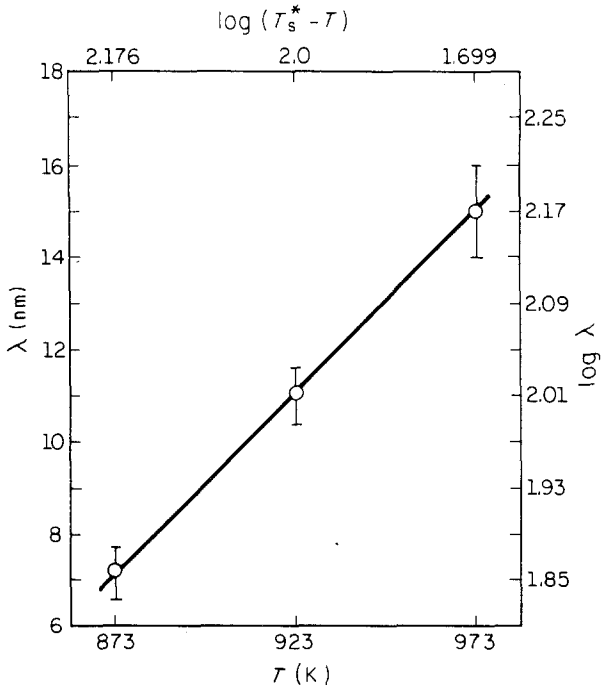

Figure 8 Plot of temperature dependence of the wavelength of decomposition for the ternary Co–3% Ti–2% Nb alloy.

4.65×10^{-21} m^2 s^{-1} at 873 K using the equation $D = 3.0 \times \exp(-33900/T)$ m^2 s^{-1} due to Thompson [12]. The concentration, C, is given by $C = \rho_{Co} W_{Ti}/M_{Ti}$, where ρ is the density of the alloy (taken to be that of cobalt) and W and M are, respectively, the weight fraction and atomic weight of titanium, and thus turn out to be 5.5×10^{-3} mol m^{-3}. The molar volume of Co_3Ti $V_m = Na^3$ where a is the lattice parameter of this compound and N is Avogadro's number. With $a = 0.3604$ nm [25], V_m works out to 27.9×10^{-6} m^3 mol^{-1}. The rate constant, K, was evaluated from the present studies to be 2.203×10^{-32} m^3 s^{-1} at a temperature $T = 873$ K. The substitution of the above data yields 9 mJ m^{-2} for γ. In this context, it may be pointed out that in other similar alloy systems γ has a value of only 11 mJ m^{-2}, e.g. for the formation of Ni_3Ti in Ni–10% Ti [24] and Ni_3Al in Ni–13% Al [3]. In both these cases the matrix solid solution has an fcc structure and the precipitate has an $L1_2$ crystal structure, very similar to the situation in the Co–Ti system. Therefore, it is likely that the value of 9 mJ m^{-2} is much closer to the real value and Thompson [12] has overestimated the interfacial energy value in his investigation. This low interfacial energy is responsible for the high resistance to coarsening in this alloy.

3.1.1.4. Stage IV: interface incoherency. Loss of coherency of the cuboidal precipitates with the matrix was observed after ageing for long times. The minimum precipitate size, S, for the occurrence of loss of coherency is given by [19]

$$S = a \cdot a_p / \Delta a \quad (2)$$

where a and a_p are the lattice parameter of the matrix and precipitate, respectively, and Δa is the mismatch parameter. This was studied in the Co–3% Ti–2% Nb on ageing at 973 K. The equilibrium solute concentration at this temperature is estimated to be 3.24 at % when the lattice parameter of the matrix is $a = 0.3560$ nm and that of the precipitate is $a_p = 0.3604$ nm. The resulting mismatch parameter, Δa, is 0.0044 nm. Estimated average size of the precipitate for the loss of coherency is $S = 30$ nm. This value is slightly smaller than the actual value observed in the present experiments.

3.1.1.5. Stage V: discontinuous coarsening. All the binary and ternary alloys exhibited a discontinuous coarsening reaction on ageing at 873 K. The coarsening is initiated at the grain boundaries and proceeded by boundary movement into the spinodally decomposed matrix. The microstructure resulting from the reaction consists of alternate lamellae of the depleted matrix and the precipitate phase. Details of discontinuous precipitation are discussed in Section 3.5.

The relationship of the microstructural evolution of the alloys with mechanical properties (especially hardness measurement) will now be discussed.

3.2. Hardness measurement

The variation in hardness of the binary and ternary alloys with ageing time at 873 and 973 K is presented in Figs 10–12. The details of the hardness results are discussed in the following paragraphs.

3.2.1. As-quenched state

The hardness values for the as-quenched binary and ternary alloys are plotted as a function of the total solute concentration in Fig. 13. From this plot, it is clear that while the hardness of the ternary alloys with niobium additions increases linearly with the niobium content, that for alloys with iron addition is nearly constant and unaffected. The amount of lanthanum was too small (0.04 at %) to effect any measurable difference in the hardness of the alloys. This behaviour can be understood in terms of the atomic radii of the various atoms [25]: cobalt (0.1252 nm), titanium (0.1462 nm), niobium (0.1468 nm), and iron (0.1274 nm). Thus cobalt and iron atoms behave in a similar fashion while titanium and niobium behave differently. It also follows that for alloys with titanium and niobium additions, the total solute content rather than the individual concentrations is of importance in determining hardness while for those with titanium and iron additions only the titanium concentration is significant.

The microstructures of the alloys did not reveal any decomposition in the as-quenched state. Thus it can be assumed that the amount of decomposition of the supersaturated solid solution was small or negligible under the quenching conditions used. In addition, a large number of stacking faults were frequently observed which is perhaps associated with the polymorphic transformation of cobalt.

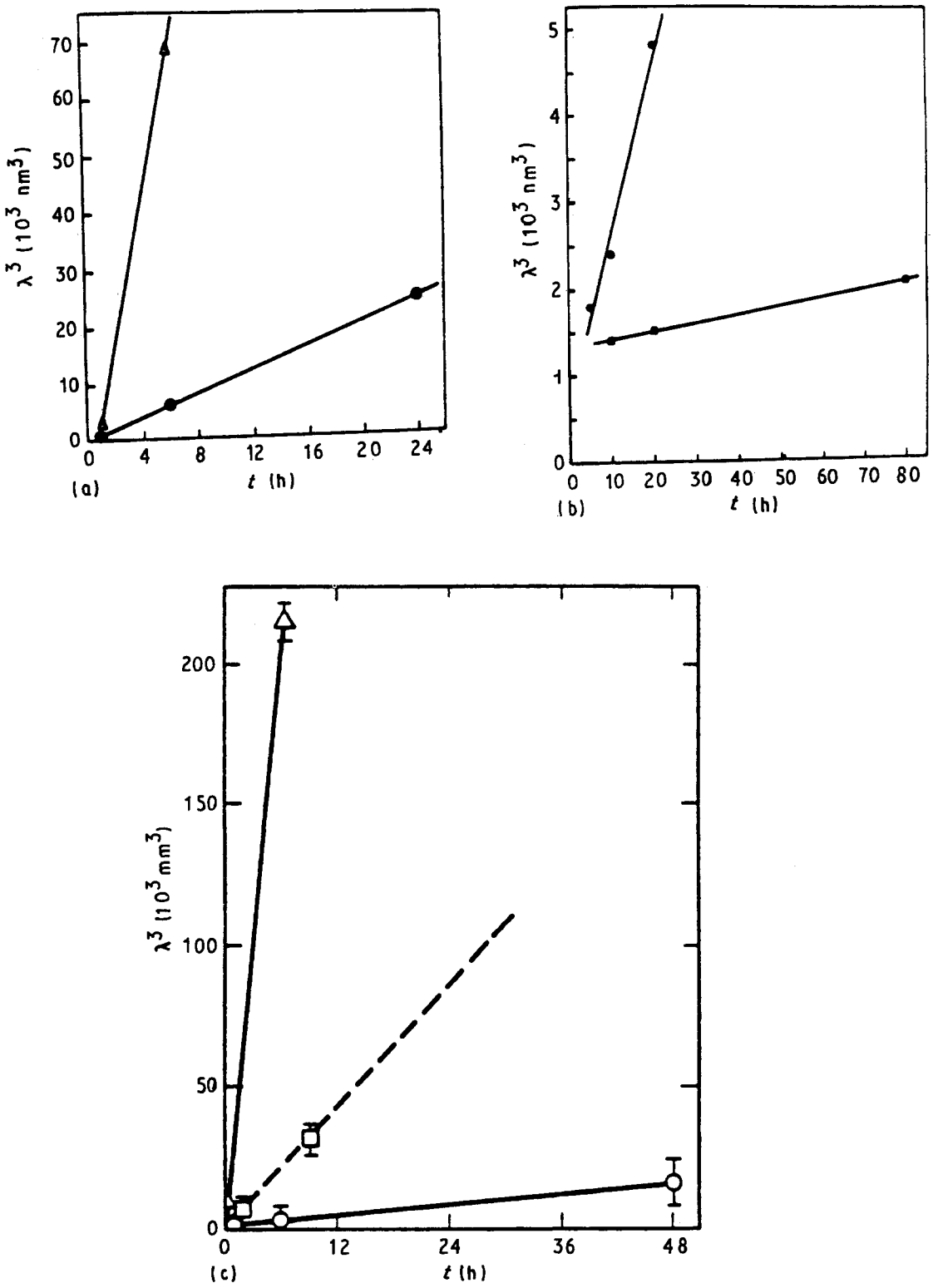

Figure 9 A plot of cube of wavelength of modulations as a function of decomposition time for the binary and ternary alloys. (a) Co–3% Ti, (●) 873 K, (▲) 923 K; (b) Co–3% Ti–0.1% La, (●) 873 K, (■) 923 K; (c) Co–3% Ti–2% Nb, (○) 873 K, (□) 923 K, (△) 973 K.

3.2.2. Aged alloys

Typical age-hardening behaviour was observed for Co–3% Ti and Co–3% Ti–0.1% La alloys only at 873 K and there was hardly any increase in hardness at 973 K, Fig. 10. In contrast, addition of iron to the binary alloys does not seem to increase the hardness value in comparison with the binary alloy (Fig. 11). There is a significant increase in the hardness on ageing at 873 K but the peak hardness for the ternary Co–Ti–Fe alloy is lower than the binary alloy. There is hardly any age-hardening response at 973 K for the ternary Co–Ti–Fe alloy, Fig. 11. This is indicative of the solvus being close to these compositions in the ternary phase diagram at 973 K. As the strength of alloys with periodic distribution of phases is strongly dependent on the variation of lattice parameter in the matrix and precipitate [26, 27], it appears that iron influences this variation so as to reduce the strength. Although the peak hardness is achieved in about 24 h for the binary and ternary alloys, the detailed kinetics are also different for the binary and ternary alloys at 873 K. The rate of increase of hardness for the ternary

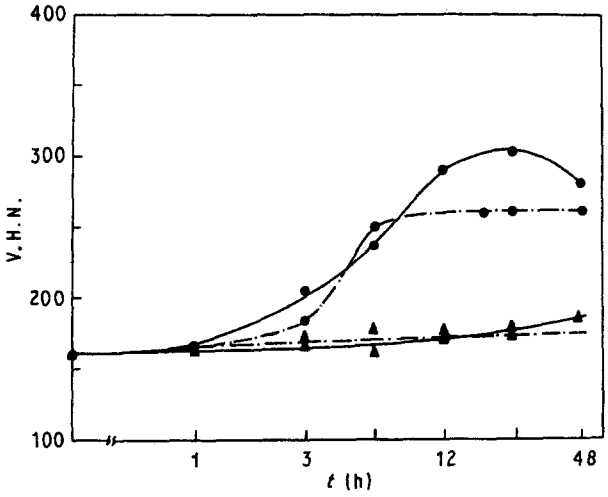

Figure 10 Isothermal hardness curves of (——) Co–3% Ti and (— · —) Co–3% Ti–0.1% La alloys aged (●) 873 and (▲) 973 K.

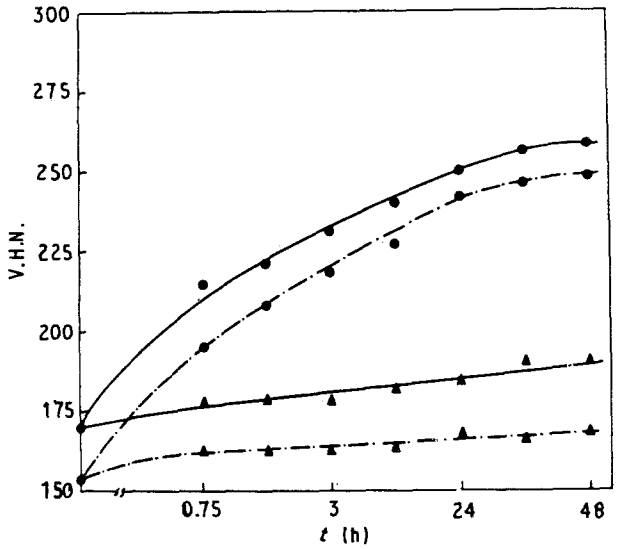

Figure 11 Isothermal hardness curves of (— · —) Co–3% Ti–1% Fe and (——) Co–3% Ti–2% Fe alloys aged (●) 873 and (▲) 973 K.

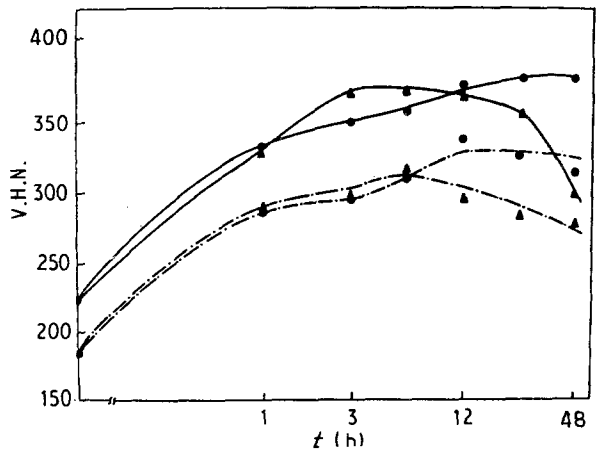

Figure 12 Isothermal hardness curves of (— · —) Co–3% Ti–1% Nb and (——) Co–3% Ti–2% Nb alloys aged (●) 873 and (▲) 973 K.

alloys is nearly constant up to the peak which is rather flat. In fact, significant overageing was not observed even when measurements were extended for ageing up to 30 days. On the other hand, the binary alloy exhibited a very slight increase in the hardness reflecting slow initial decomposition followed by rapid attainment of the peak and overageing. This behaviour can arise due to several factors discussed by Cahn [28]. Microstructural evidence shows that loss in hardness on overageing is associated primarily with a coarsening of the periodically modulated structure and with discontinuous coarsening in the case of the ternary Co–Ti–Fe alloy.

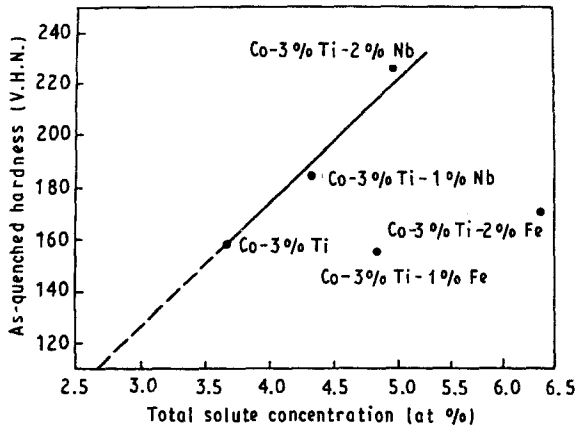

Figure 13 Plot of variation in hardness with solute concentration for as-quenched (single-phase) alloys.

Addition of niobium to the binary alloy seems to have a remarkable effect on age hardening at both the ageing temperatures (873 and 973 K), Fig. 12. Approximately two-thirds of the total hardness increase occurs within 1 h of ageing for the ternary alloys, whereas for the binary alloy, the time required for a similar increase is about 10 h after ageing at 873 K. Although an increase in the rate of decomposition is expected for increasing amount of solute content even for decomposition by nucleation and growth mechanism, it appears that the dramatic increase observed in this case is associated with the spinodal mode of decomposition. The absence of an activation barrier in the spinodal decomposition is expected to lead to an increased rate of decomposition in comparison to that for precipitation by nucleation and growth mechanism which requires an activation energy for nucleation.

Based on microstructural evolution of the aged alloys, the peak hardness of the alloys corresponds to the third stage of precipitate coarsening (precipitate coarsening stages are discussed in the next section). The difference in these values for the various alloys and the two ageing temperatures can be explained as follows. The solid solution hardening is first estimated by utilizing the known solubility in conjunction with Fig. 13. The incremental hardness (peak hardness less solid solution hardening) can thus be obtained and is shown as a function of the square root of the volume fractions of the precipitating phase in Fig. 14. These volume fractions were obtained by quantitative transmission electron microscopy and are found to be in reasonable agreement with those calculated from the phase diagrams. Except for Co–3% Ti–2% Nb alloy aged at 973 K, all the other data points satisfy a linear relationship. This behaviour is expected for strengthening due to coherent precipitate particles

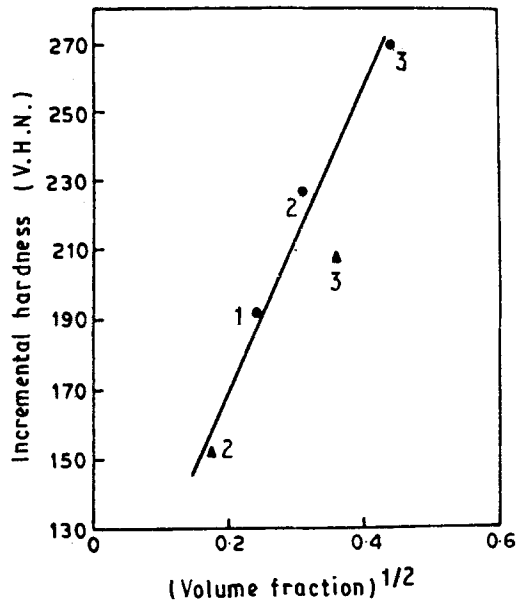

Figure 14 Plot of variation in hardness with volume fraction of the precipitates for two-phase alloys: 1, Co–3% Ti; 2, Co–3% Ti–1% Nb; 3, Co–3% Ti–2% Nb. (●) 873 K, (▲) 973 K.

TABLE II Tensile properties of Co–3% Ti

Ageing temp. (K)	Ageing time (h)	YS (MPa)	UTS (MPa)	%El.
Solution treated		136	348	17
873	24	298	564	8
873	48	176	618	15
973	3	267	438	8
973	6	218	361	6
973	24	195	509	16

TABLE III Tensile properties of Co–3% Ti–2% Nb alloy

Ageing temp. (K)	Ageing time (h)	YS (MPa)	UTS (MPa)	%El.
Solution treated		238	538	35
873	12	322	1093	13
873	48	303	1041	15
973	6	588	1021	15
973	24	270	980	14

TABLE IV Yield strength (0.2% offset) for alloys aged at 873 K

	Yield strength (MPa)	
Ageing time (h)	Co–3% Ti–1% Nb	Co–3% Ti–2% Nb
0	197	216
0.75	296	374
6	424	384
24	433	473
96	443	482

[29]. The details of strengthening mechanisms in spinodally decomposed alloys will be discussed in the next section. Mechanical properties of the binary and ternary alloys are presented in Tables II–IV. The behaviour of the yield strength is similar to that of hardness and can be explained on the same basis.

3.3. Strengthening mechanisms

Spinodal decomposition can lead to high strengths. Different strengthening mechanisms may be expected to operate in the case of coherent and semi-coherent precipitates which will be briefly reviewed below.

In the case of a coherent spinodal product, no comprehensive theory of strengthening during the early stage of ageing exists. Cahn's model [30] is strictly applicable to early stages of ageing when an approximately sinusoidal composition profile exits. The analysis is essentially applicable to the interaction of slip dislocations with a microlattice of periodically varying obstacles regardless of the origin of the modulated structure. Cahn's internal strain-hardening model predicts a rising part of the ageing curve proportional to λ, the wavelength of the modulated structure and a branch which falls off as $\lambda^{-2/3}$. The rising branch is the analogue (or modification) of the Mott–Nabarro theory [31] and the falling branch is the analogue of the Orowan hardening mechanism [32]. The model identifies two domains defined by extreme values of the parameter $P = A^n Y\boldsymbol{b}/\gamma\beta$, where A is the amplitude of the composition fluctuation or modulation, n a distortion parameter $= \partial \ln a/\partial C$, Y Young's modulus, $\boldsymbol{b}$ Burgers vector, γ the line tension of the dislocations, and β the wave vector $= 2\pi/\lambda$. For $P > 1$, a dislocation can curl around the pseudo-particles of composition extreme and produce Orowan-type hardening in the structure. In all spinodal alloys examined to date, usually $P < 1$ and for this, the critical resolved shear stress is [30]

$$\sigma_c = A^2 n^2 \gamma^2 \boldsymbol{b}/3\sqrt{6\gamma\beta} \quad \text{(for screw dislocations)} \tag{3}$$

This theory states that for a given alloy, the incremental yield stress will be $\Delta\sigma \propto A^2\beta^{-1} \propto A^2\lambda$. Thus, a critical test of the theory depends on measuring the values of λ and A.

Recent analysis suggests that the yield strength varies directly with the difference in composition of the two decomposing phases and is independent of the interparticle spacing, volume fraction of the spinodal product and wavelength of the composition, and is given by [18, 33, 34]

$$\sigma_{YS} = m/3\sqrt{6}(C_{11} + C_{12} - 2C_{12}/C_{11})\Delta a/a_0 \tag{4}$$

where m is the Taylor factor for converting from single-crystal shear stress to polycrystalline tensile stress, C_{ij} are the single-crystal elastic stiffness constants and Δa is the difference between a and a_0 the average of the cubic lattice parameters of the precipitating phases.

During the later stages of spinodal decomposition, the precipitating phases have compositions approaching the equilibrium ones. At this stage, the elastic strains become sufficiently large and lead to a loss of coherency by the generation of interfacial misfit

dislocations. These interfacial dislocations are arranged periodically at distances equal to the wavelength of the prior coherent precipitates. Thus, during plastic deformation, the slip dislocations encounter the interfacial dislocations and additional stress will be required to overcome the interaction between the two. The maximum distance a slip dislocation travels between encounters with the two walls of interfacial dislocations is $\sqrt{2}\,Z$ where Z is the spacing of the misfit dislocations. Usually λ would be a small multiple of Z.

If both the phases have equal elastic moduli, the slip dislocations can move through both phases by overcoming the barrier presented by the interfacial dislocations. On the other hand, if one of the phases is harder compared to the other, then slip dislocations will tend to move only within the softer phase by finding routes around the harder phase. The interface can be considered similar to grain boundaries because the periodic arrays of misfit dislocations are stable [35]. As a consequence, Hall–Petch strengthening may be expected with the yield strength proportional to $Z^{-1/2} \approx \lambda^{-1/2}$ if $Z = \lambda$. Thus this transformation presents a unique route for synthesis of a microstructure, periodic in dimensions and periodic in the distribution of dislocations.

An attempt has been made to estimate the incremental yield stress due to spinodal decomposition. To rationalize the results, it has been assumed that the Co–3% Ti–2% Nb alloy behaves like a Co–4.96 at % Ti alloy, i.e. no distinction is made between the titanium and niobium atoms. The value of Δa for this calculation has been obtained from the equilibrium data of Fountain and Forgeng [4]. The average lattice parameter of the solid solution, a_{ss}, has been obtained by fitting a parabolic equation to these data as follows

$$a_{ss}(\text{nm}) = b_0 + b_1 c + b_2 c^2 \quad (5)$$

where c is the concentration in atomic fraction and b_0, b_1, and b_2 are constants. A rough estimate of the concentration of the solute poor regions can be made by utilizing the coherent spinodal temperatures reported above for the Co–3% Ti and Co–3% Ti–2% Nb alloys. Thus, this concentration is taken to be higher than the equilibrium concentrations by 1% and a_{ss} works out to be 0.355 89 nm.

3.4. Solvus composition estimation

After long ageing times, the volume fraction, V_v, of the precipitate was determined by quantitative transmission electron microscopy utilizing approximate corrections for overlap as follows

$$V_v = V'_v/1 + \frac{3}{2}t/D \quad (6)$$

where the foil thickness, t was estimated to be 60 nm and the apparent volume fraction, V'_v, and the precipitate size, D, were measured in each case. The values so found are given in Table V. Utilizing the known composition of the Co_3Ti precipitate in equilibrium with the solid solution from the work of Fountain and Forgeng [4], the equilibrium solvus composition has been evaluated from the volume fraction, assuming that (1) the densities of the phases are identical and (2) no distinction be made between titanium and niobium. The averages of these are also included in the table. These values are in good agreement with the equilibrium phase diagram for Co–Ti constructed by Fountain and Forgeng [4]. To enable estimation of the solvus composition required elsewhere analytically, we have expressed the same as follows

$$C_e = A\exp(-B/T) \quad (7)$$

where C_e is the solvus composition (at %) and A and B are constants. Utilizing the results in Table V, the maximum solubility of titanium in cobalt is estimated to be 12.85 at % at 1473 K. The temperature corresponding to a solvus composition of 2.9 wt % Ti is 995 K which is between 973 and 1073 K and this is in conformity with the phase diagram of Fountain and Forgeng [4].

As shown for Co–3% Ti aged at 973 K for 360 h in Fig. 1, Moiré fringes are occasionally observed. These arise due to the small difference in lattice parameters of the precipitate and the matrix, and are thus displacement type. Measurement of the fringe spacing yielded the lattice parameter difference $\Delta a = 0.0033$ nm. As mentioned earlier this is expected to be 0.0042 nm on the basis of numerical analysis of the solvus compositions and the lattice parameters found by Fountain and Forgeng [4]. The agreement between these values is considered to be satisfactory.

3.5. Discontinuous precipitation

The distinction between continuous and discontinuous precipitation is shown schematically in Fig. 15. In the continuous mode of precipitation, there is a continuous change in composition as well as the lattice parameter of the matrix phase, α_0, as a function of time. In addition, the precipitating phase, β, is uniformly distributed within the matrix. On the other hand, in discontinuous precipitation, there is a sudden

TABLE V Volume fraction of precipitate particles determined by quantitative transmission electron microscopy

Temperature (K)	Volume fraction		Calculated average solvus Composition (at %)
	Co–3% Ti	Co–3% Ti–2% Nb	
873	0.055	0.180	2.17
923	0.222	–	–
973	0.017	0.130	2.69

TABLE VI Growth and diffusion data for binary and ternary alloys [36]

Temperature (K)	G (m s^{-1})			D' (m^2 s^{-1})			D_v^z (m^2 s^{-1})	D_v^{mz} (m^2 s^{-1})	D_b^l (m^2 s^{-1})	D_b^{mt} (m^2 s^{-1})
	Co–Ta [49]	Co–Mg [50]	Co–Ti–Nb	Co–Ta [49]	Cr–Co [50]	Co–Co [49]	Equation 13	Equation 14	Equation 15	Equation 16
873	–	–	0.33×10^{-10}	–	–	–	0.15×10^{-16}	0.20×10^{-16}	0.17×10^{-15}	0.55×10^{-16}
923	1.1×10^{-10}	0.5×10^{-8}	0.43×10^{-10}	7.0×10^{-20}	4.0×10^{-20}	8.0×10^{-21}	0.34×10^{-16}	0.35×10^{-16}	0.53×10^{-15}	0.13×10^{-15}
973	4.2×10^{-10}	0.8×10^{-7}	0.52×10^{-10}	3.4×10^{-19}	2.5×10^{-19}	5.0×10^{-16}	0.88×10^{-16}	0.61×10^{-16}	0.24×10^{-14}	0.47×10^{-15}
1023	4.1×10^{-9}	0.2×10^{-7}	0.38×10^{-10}	3.5×10^{-18}	5.0×10^{-18}	2.5×10^{-19}	0.13×10^{-15}	0.54×10^{-16}	0.56×10^{-14}	0.84×10^{-15}
1073	9.1×10^{-9}	0.8×10^{-7}	–	9.5×10^{-18}	2.0×10^{-18}	1.0×10^{-18}	–	–	–	–

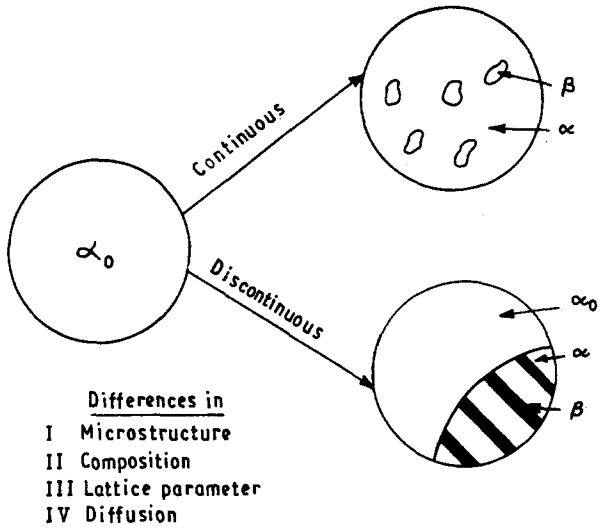

Figure 15 Schematic illustration of continuous and discontinuous type precipitation.

change in the composition as well as lattice parameter of the depleted matrix phase, α, across the interface. The microstructure consists of alternate lamellae of the precipitating phase, β, and the depleted matrix phase, α, which originate heterogeneously at grain boundaries or dislocations. Further, the diffusion distance in the case of discontinuous precipitation is relatively smaller (~ 1 μm) than that in continuous precipitation.

All the alloys have shown discontinuous precipitation on ageing between 823 and 1023 K. Therefore, detailed investigation would be mainly focused on the Co–3% Ti–2% Nb alloy and results would be compared with binary Co–3% Ti and the ternary Co–3% Ti–2% Fe alloys. The early stage of growth of discontinuous precipitation in the ternary Co–3% Ti–2% Nb alloy aged at 923 K for different times was investigated by TEM and the results are shown in Fig. 16. Fig. 16a reveals a high density of closely spaced allotriomorphs at the grain boundary. The grain boundary is almost straight. In addition, cuboid precipitates are present in the matrix. The advanced growth of a discontinuous cell is shown in Fig. 16b–d. The precipitate lamellae were identified as Co_3Ti, an ordered phase. On ageing for longer times, discontinuous precipitates grew to such a large size that precipitates could be seen even by optical metallography. A typical optical micrograph of the discontinuous precipitates observed in the Co–3% Ti–2% Nb alloy aged at 873 K for 290 h is presented in Fig. 17. Discontinuous precipitates were observed only at high-angle boundaries and not at low-angle boundaries or twins. The growth of the discontinuous product was found to be different at each side of the grain boundary and also within the twinned regions. The maximum displacement of the interface of discontinuous precipitation at different temperatures is plotted as a function of time in Fig. 18 and the growth rates as a function of temperature for some of the alloys are displayed in Fig. 19. The growth rate of discontinuous precipitation increased with increasing ageing temperature up to its maximum growth rate

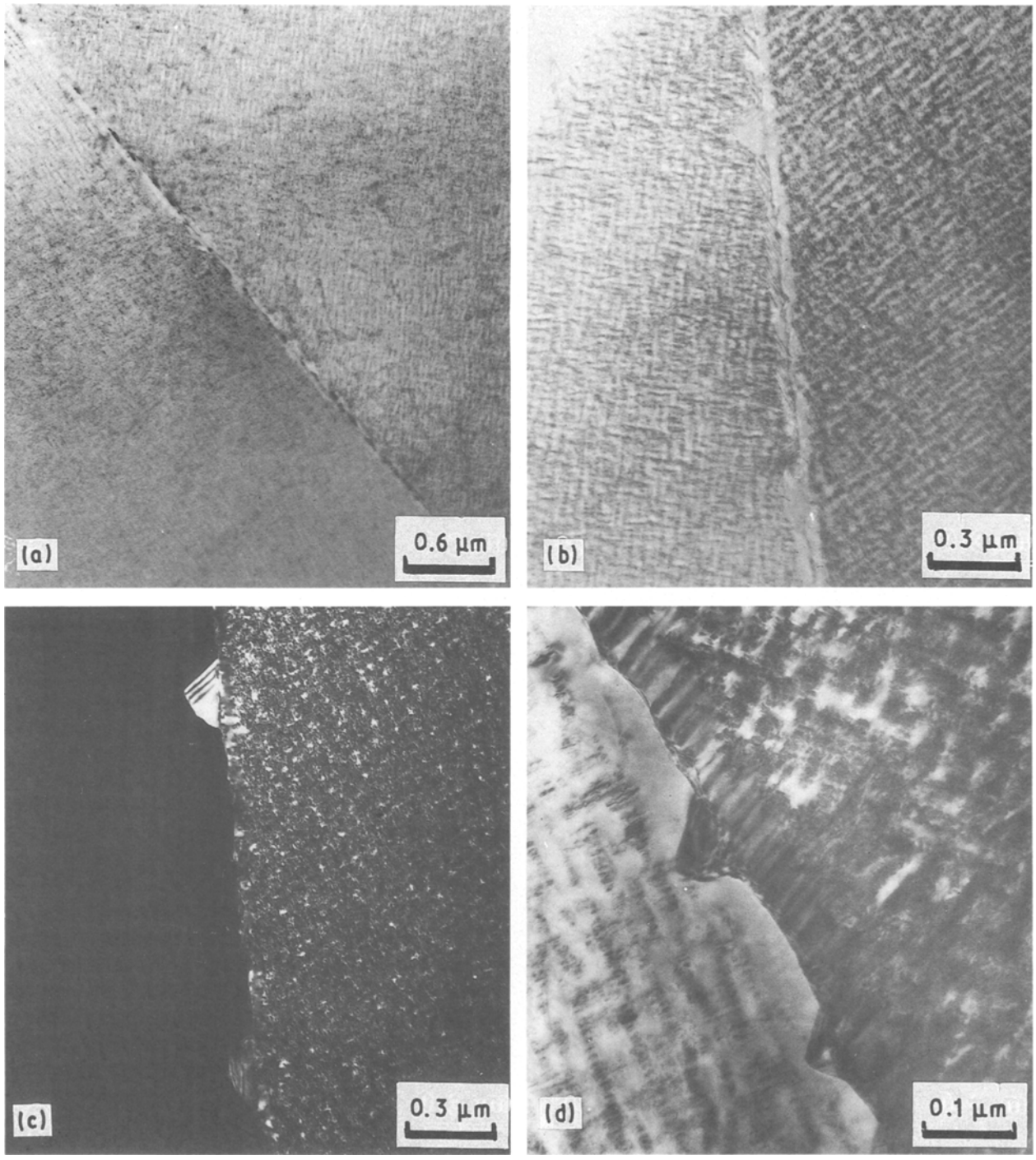

Figure 16 Transmission electron micrographs of Co–3% Ti–2% Nb alloy aged at 923 K for different times showing the growth of discontinuous cell for (a, b) 120 h and (c, d) 240 h.

(i.e. up to the nose of the curve). The maximum migration rate of the discontinuous front in the binary Co–3% Ti, and ternary Co–3% Ti–2% Fe and Co–3% Ti–2% Nb alloys was found to occur at 923, 873 and 973 K, respectively. However, at higher ageing temperatures (i.e. above the nose temperature), the growth rate decreased and finally dropped to zero. The upper temperature limit for the occurrence of discontinuous precipitates was found by plotting the reciprocal of interlamellar spacings for the binary and ternary alloys as a function of ageing temperature as shown in Fig. 20. Extrapolation of these lines to zero interlamellar spacing (i.e. absence of discontinuous precipitation) shows the upper temperature limit for the occurrence of discontinuous precipitation for Co–3% Ti, Co–3% Ti–2% Fe, and Co–3% Ti–2% Nb alloys as 973, 923, 1073 K, respectively. This indicates that addition of niobium to the binary alloy increased the upper temperature limit for the occurrence of discontinuous precipitation, whereas iron had shown the opposite trend [36].

On ageing the Co–3% Ti, Co–3% Ti–2% Fe and Co–3% Ti–2% Nb alloys at higher temperatures (e.g. 973 K for 170 h, 923 K for 192 h, and 1073 K for 360 h, respectively) discontinuous precipitates were not observed and only grain boundary and general matrix precipitation were observed (Fig. 6). General matrix and grain-boundary precipitation in both Co–3% Ti

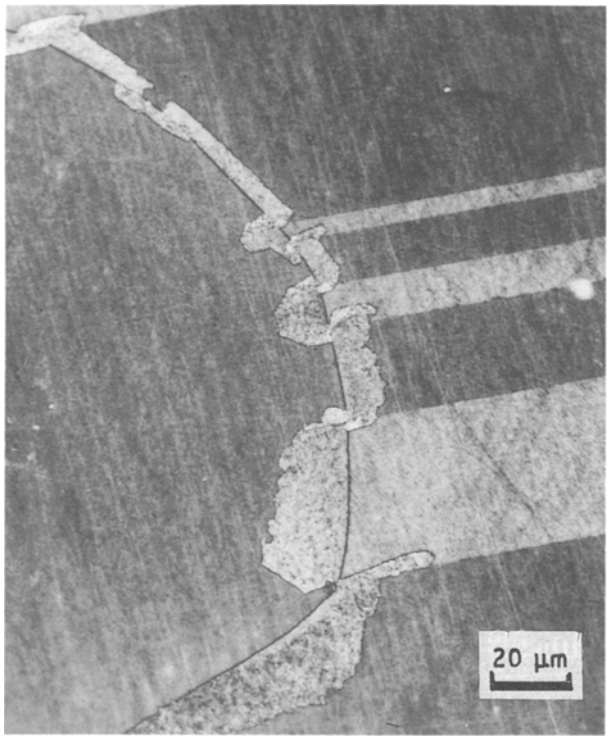

Figure 17 Optical micrograph of Co–3% Ti–2% Nb alloy aged at 873 K for 290 h showing the effect of crystallographic orientation on the discontinuous precipitation.

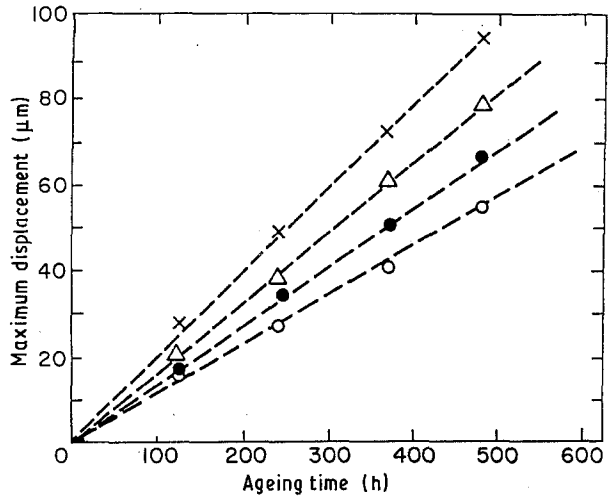

Figure 18 A plot of maximum displacement of a discontinuous cell at different temperatures as a function of time in Co–3% Ti–2% Nb. (○) 873 K, (△) 923 K, (×) 973 K, (●) 1023 K.

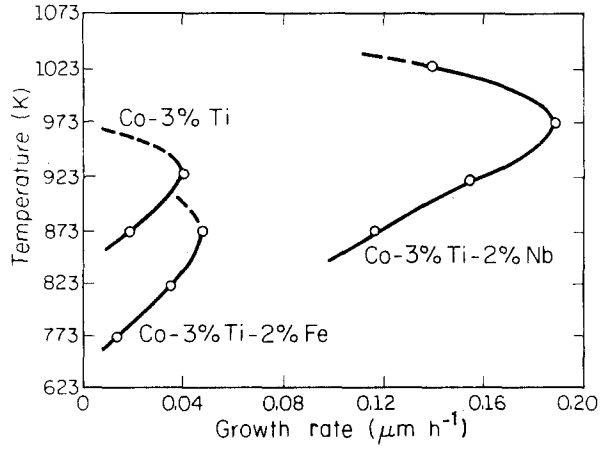

Figure 19 A plot of growth rate versus time for Co–3% Ti, Co–3% Ti–2% Fe and Co–3% Ti–2% Nb alloys.

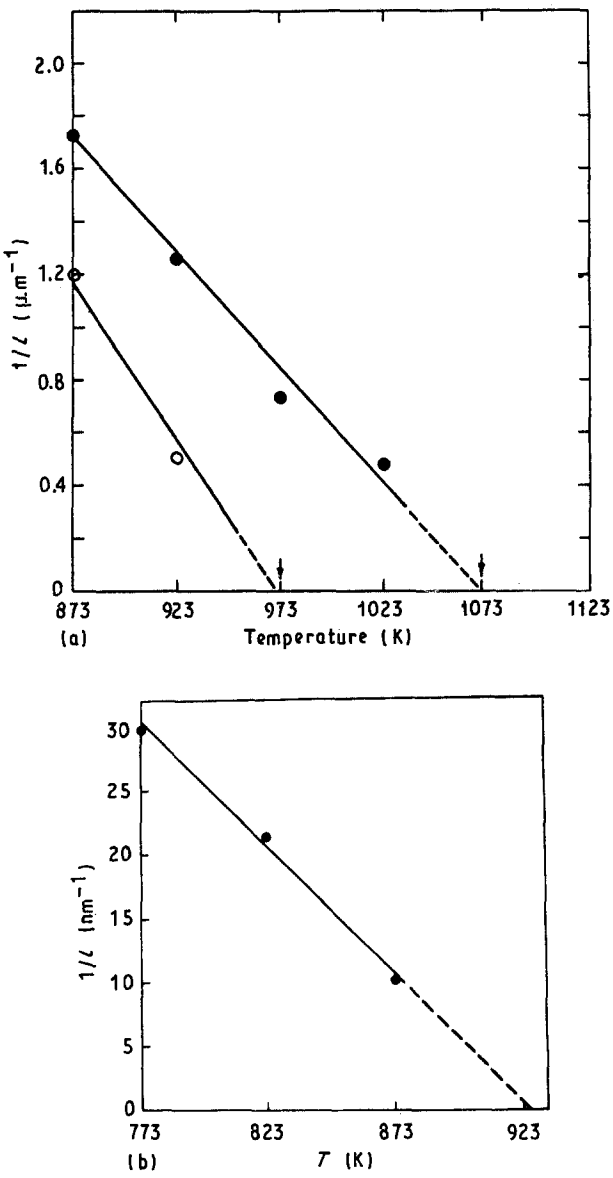

Figure 20 A plot of reciprocal interlamellar spacing versus temperature for alloys. The extrapolation shows the upper temperature limit for discontinuous precipitation. (a) (○) Co–3% Ti, (●) Co–3% Ti–2% Nb. (b) Co–3% Ti–2% Fe.

and Co–3% Ti–2% Fe alloys appeared to be the same. In addition, both the alloys show grain-boundary precipitation along with precipitate-free zones. Comparatively, precipitate morphology in the Co-3% Ti–2% Nb alloy appeared to be different. However, experimentally determined temperatures at which discontinuous precipitation was absent, are the same as those obtained by extrapolation (Figs 6 and 20).

In order to determine the composition profile between the lamellae in the discontinuous product, microanalysis of the samples was carried out in the STEM using quantitative X-ray spectroscopy. This analysis was performed in the stationary spot mode, thus permitting longer counting times and consequent reduced statistical uncertainty. The composition profiles of the lamellae in the discontinuous product of

binary Co–3% Ti and ternary Co–3% Ti–2% Nb alloys are presented in Fig. 21a and b, respectively. The composition gradient between the lamellae is flat indicating that depleted matrix and lamellae have reached the equilibrium conditions.

Each of the several methods of observations employed in this study contributes to an overall view of the transformation. From the optical metallographic studies, we note that the maximum growth of discontinuous precipitate is a function of temperature, time and interlamellar spacing at a given temperature (Figs 19 and 20). In addition, there is also a major influence of anisotropy on the migration front of discontinuous precipitation as reflected in the irregular cusped or faceted morphologies. We consider that the development of these facets is a direct consequence of the structure sensitivity of the boundary migration (Fig. 17). This pronounced structure sensitivity is closely related to the small driving force under which the front propagates. This is discussed more fully in subsequent sections.

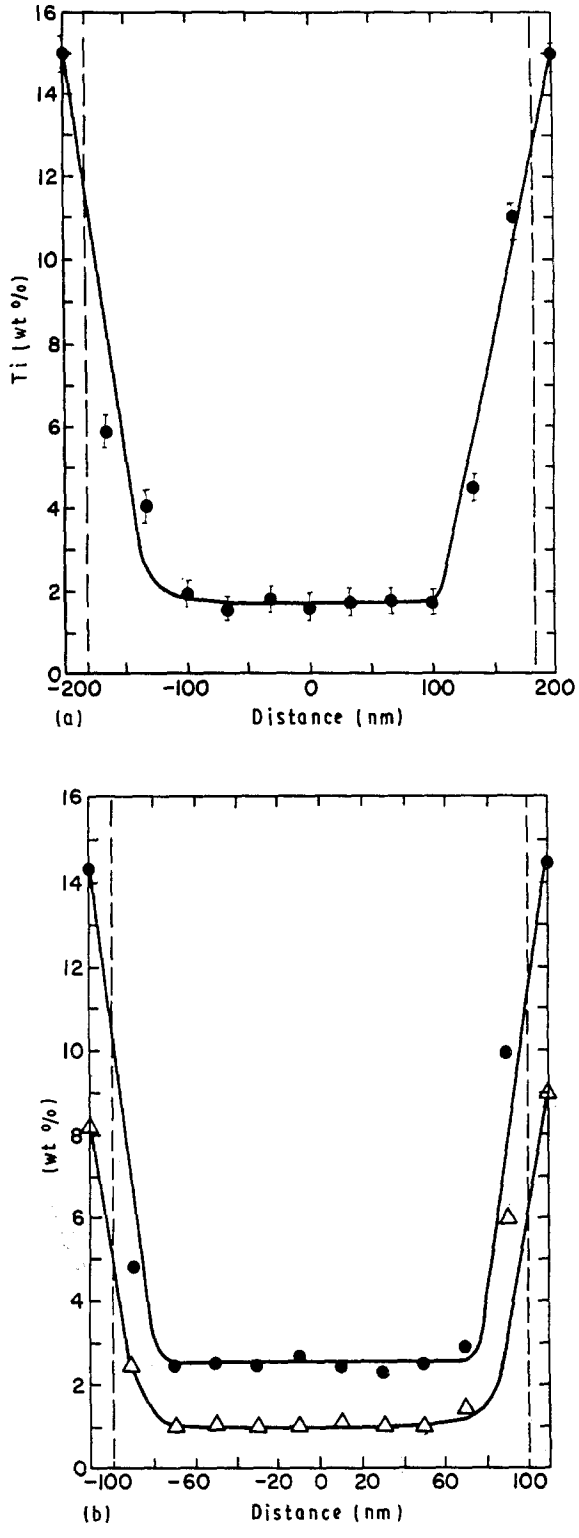

Figure 21 Composition profile between the lamellae in the discontinuous product in (a) Co–3% Ti aged at 873 K, and (b) Co–3% Ti–2% Nb alloy (●) Ti, (△) Nb, aged at 973 K.

From the TEM microstructural evolution it is now possible to say that initially the alloy decomposed by a spinodal mode followed by coarsening of coherent Co_3Ti type intermetallic compound. These compounds are always under nonequilibrium conditions. For the time and temperature under study, there is a competition taking place between the nonequilibrium spinodally decomposed product and discontinuous precipitation. At a well advanced stage, the parent phase mixture seen by the discontinuous transformation front is very close to the full coherent equilibrium, as modified slightly by capillarity between Co_3Ti cuboids or $Co_3(Ti, Nb)$ discs and depleted cobalt-rich solid solution. Microstructural (Fig. 16) and microchemical (Fig. 21) studies of the quenched transformation interface and its environment demonstrate that

1. the local interfacial curvature between Co_3Ti precipitates is uniform and small;
2. the interface tends to bow slightly towards the parent phase matrix; and
3. the concentration profile in the depleted α phase immediately behind the transformation front is essentially flat.

These observations, taken together, provide strong indication that the local driving force is essentially uniform along the grain-boundary segments between discontinuously formed plates or rods. This supports the recent findings in Al–Zn [37] and Mg–Al [38] alloys, and is consistent with the high-temperature behaviour of dilute Cu–Co alloys [39] where coherent rods form discontinuously from the matrix of coherent cobalt spheres in a depleted copper-rich matrix.

3.5.1. Driving forces

We shall now discuss the different local driving forces operating in the discontinuous precipitation.

The precipitate rods or plates in the discontinuous product have evidently lost full coherency (Fig. 16). Thus the main driving force for discontinuous precipitation is the difference between coherent and incoherent free energies of the two-phase mixture. This contention is consistent with the observations that discontinuous precipitation is absent in alloys where the general precipitates are incoherent or semi-coherent (Fig. 6) and that the maximum velocity and the spacing are constant with time for a given alloy and reaction temperature. These observations and arguments place the transformation firmly in the low driving force category. Different driving forces operating in the discontinuous reactions are: (1) chemical driving

force; (2) coherency driving force; (3) capillarity driving force.

3.5.1.1. Chemical driving force. The chemical driving force on the reaction front in discontinuous precipitation is available due to the fact that transport of solute atoms through the grain boundary is much faster than the given volume diffusion ($D_B > D_V$). Thus there exists a concentration difference at the moving boundary interface. This available chemical difference or driving force will induce the boundary to migrate. According to Hillert's formulation [40], the chemical driving force, p^{chem}, is given by

$$p^{chem} = f\Delta G^{diff}/V_m \quad (8)$$

where $\Delta G^{diff} = RT(X_0 - X_e)^2/V_m 2X_0$. Here, dilute solid solution behaviour is assumed and X_0 is the composition of the supersaturated alloy and X_e is its equilibrium concentration. ΔG^{diff} is the driving force energy due to diffusion per molar volume, V_m, and f is the fraction of driving force energy.

Because the concentration step is moderated by volume diffusion, the fraction of this force, f, available for boundary migration can be estimated from

$$f = 1 - \exp(-vb/2D_v) \quad (9)$$

where v is the growth velocity, and b is interatomic distance. For the Co–3% Ti binary alloy aged at 873 K, $X_e = 1.5$ wt % Ti, $b = 0.5$ nm, $D_v = 4.65 \times 10^{-21}$ cm^2 s^{-1}, $V_m = a_0^3 N \approx 27.897 \times 10^{-10}$ m s^{-1} and $R = 10$ J K^{-1} mol^{-1}. Thus, $\Delta G^{diff} = 11.73 \times 10^7$ J m^{-3}, and $f = 0.607$.

3.5.1.2. Coherency force. At temperatures where volume diffusion dominates, the local force for grain-boundary migration may have another source called coherency force [39]. Coherency stresses are due to composition gradient developed in the depleted zone ahead of the boundary. The coherency stress is then due to the variation of lattice parameter, Δa, with composition and is given by the misfit parameter, η

$$\eta = d\ln a/dc \quad (10)$$

3.5.1.3. Capillarity force. Pervoic and Purdy [39] suggested two kinds of capillarity forces acting on the grain boundary:

(a) a grain growth force arising from the initial curvature of the boundary;

(b) a "tractional force" due to the tendency of growing precipitate to pull the boundary into such a shape that the boundary curvature assists growth.

If the grain growth force is only operating during the formation of rod colonies, one would expect to find all grain boundaries migrating towards their centre of curvature. This is not always observed, especially in the present alloys. In such cases, traction force is also believed to be operating as the precipitate grows. This resulting force is given by

$$F = N2\pi r_0\gamma \quad (11)$$

where N is the number of rods per unit area, r_0 is the rod radius and γ is the surface energy of the newly formed rod–matrix interface which is the same as that for Co_3Ti cuboids in the matrix of the binary Co–3% Ti alloy (which is about $\gamma = 9$ mJ m^{-2}). Thus, the estimated value of F is 6.8×10^3 J m^{-3}.

If the lamellae of the discontinuous product are assumed to be rods, then the volume fraction will be determined by the composition of rod of radius, r_0, and the spacing, l, between rods. For a given rod radius, r_0, the volume fraction of lamella rod is $\pi r^2 N$, where N is the number of rods per unit area, and $N = 1/l^2$, so that, the volume fraction becomes [39]

$$V_f = \pi r_0^2/l^2 \quad (12)$$

For the Co–3% Ti alloy aged at 873 K, the volume fraction of the cuboid precipitates in the matrix is estimated to be 0.055 while a rod dispersion with radius $r_0 = 0.05$ μm, would yield a volume fraction 0.011, in good agreement with the observed spacings.

3.5.2. Nucleation of discontinuous precipitation

Three important models have been proposed for the initial boundary migration: (1) a pucker mechanism in which the formation of faceted nuclei/precipitates at the grain boundaries is the requirement (due to Tu and Turnbull [41]), (2) free boundary migration, in which boundary curvature is required (due to Fournelle and Clark [42]), and (3) grain-boundary precipitate induced migration in which "unpinning" of the boundary segment takes place (due to Lange and Purdy [43]).

In order to see which of the above models is applicable to cobalt-based alloys, it is necessary to see the initiation of discontinuous precipitation, as displayed in Figs 16 and 17. The initiation of discontinuous precipitation involves copious grain-boundary precipitation in the form of globular, incoherent or semi-coherent allotriomorphs of a stable precipitate. The intragranular precipitates possessing coherency strain fields are less stable than the grain-boundary allotriomorphs; a chemical potential difference thus exists for the migration of solute atoms from the nearby cuboid precipitates to the grain-boundary allotriomorphs, once coarsening conditions are established. As the grain-boundary precipitates coarsen by competition among themselves and by competition with neighbouring intergranular precipitates, the boundary regions between them will become enlarged. Thus, the coarsening process required to "unpin" the boundary segments will probably take place very close to equilibrium and in the absence of significant local matrix supersaturation. For the present case, the matrix near the grain boundary must closely approach the incoherent equilibrium solute content at the time of initiation, which is inclined to favour an initiation mechanism involving a precipitate traction, perhaps of the type proposed by Lange and Purdy [43] in which the initial displacement occurs when a segment of boundary pulls away from a shrinking precipitate (Fig. 22).

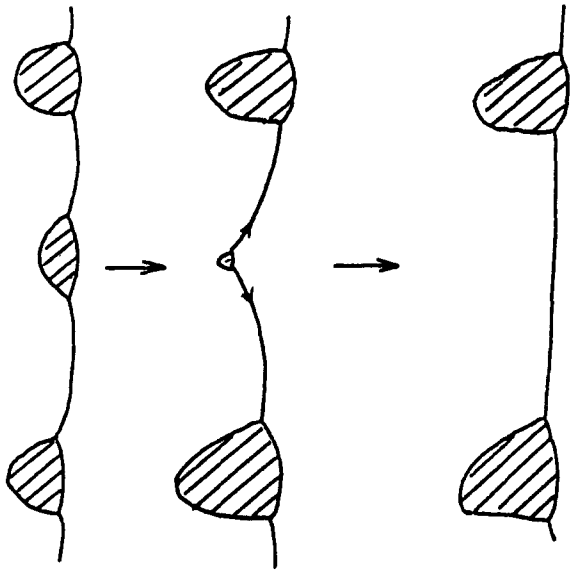

Figure 22 Nucleation and growth of discontinuous cell morphology according to Lange and Purdy [43].

3.5.3. Cell growth kinetics

In order to determine the rate-controlling factor in the reaction growth, it would be desirable to study the change in solute content across the advancing interface. Volume diffusion control reaction of Zener's type should result in a classical diffusion profile into the supersaturated solid solution (as presented in Fig. 21a of [44]) while boundary-controlled reaction would result in a discontinuous change in composition profile across the interface (as presented in Fig. 21b of [44]). There were competitive reactions involving the general fine and uniform homogeneous precipitation (i.e. spinodal decomposition) and coarsening of coherent Co_3Ti type intermetallic compound in the matrix and ahead of the interface of discontinuous precipitation.

It is very difficult to measure the composition profile ahead of the interface in cases as discussed above. In such cases various models for the cell growth would be tested using experimental data and they are discussed below.

The cell growth rate, G, is given by Zener's equation, when the cell growth is controlled by volume diffusion mechanism [45]

$$G = 2\frac{(X_0 - X_e)D_v^z}{X_0 l} \tag{13}$$

where D_v^z is the volume diffusion coefficient of titanium solute atoms in the cobalt matrix, X_0 and X_e are the initial solute concentration and equilibrium concentration of depleted matrix, respectively, and l is the interlamellar spacing. In addition to discontinuous precipitation, continuous precipitation also occurred in the matrix of binary and ternary alloys; therefore, Zener's modified equation proposed by Aaronson and Clark [46] should be tested and is given by

$$G = \frac{(X_m - X_e)(X_\beta - X_e)2D_v^{mz}}{(X_\beta - X_0)(X_0 - X_e)l} \tag{14}$$

where X_m is the matrix composition ahead of the

TABLE VII Comparison of activation energies and D_0 values [36]

	Q (kJ mol^{-1})					D_0^{Co-Co} (m^2 s^{-1})	
	Co–Co [21]	Co–Ti–Fe	Cu–Mg [50]	Co–Ti–Nb		[21]	Calculated
Volume (v)	243	331 [51]	234	319 [36]		3.0×10^{-7}	Eq. 13: 0.94×10^{-10} Eq. 14: 0.39×10^{-13}
Boundary (b)	117	234 [36]	139	113 (Eq. 13)	54 (Eq. 14)	178 (Eq. 15)	140 (Eq. 16)	1.2×10^{-7}	Eq. 15: 0.75×10^{-5}
$\frac{Q_b}{Q_v}$	0.48	0.7	0.6	0.35 (Eq. 13)	0.17 (Eq. 14)	0.56 (Eq. 15)	0.44 (Eq. 16)		Eq. 16: 0.14×10^{-7}

interface and X_β is the composition of the second phase $Co_3(Ti, Nb)$. The activation energy, Q_v^{mz} and D_0 calculated using Equation 10 is 54 kJ mol^{-1} and 0.387 $\times 10^{-13}$ m^2 s^{-1}, respectively. The estimated D_0^v value is higher than the volume self diffusion of pure cobalt (Tables VI and VII). Therefore, the cell growth rate cannot be represented by Equations 13 and 14.

Turnbull proposed the following growth equation when cell growth is controlled by a grain-boundary diffusion mechanism [47]

$$G = \frac{2(X_0 - X_e)\Gamma D_b^T}{X_0 l^2} \quad (15)$$

where D_b is the grain-boundary diffusion coefficient and Γ is the effective thickness (≈ 50 nm). Liu and Aaronson [48] modified Turnbull's equation as follows

$$G = 4\Gamma D_b^{mt}/l^2 \quad (16)$$

The D_v, D_b, D_0 and activation values obtained from Equations 13–16 are presented in Tables VI and VII. The experimentally found values for the Co–3% Ti–2% Nb alloy are compared with those for other binary alloys. Unfortunately, diffusion data are not available for these materials and more detailed analysis is, therefore, not possible.

D_0 estimated from Equation 15 is higher than the grain-boundary diffusion for pure cobalt. Therefore, Equation 16 seemed to be more reasonable to express the cell growth in these alloys. From the above consideration, it can be concluded that the cell growth is controlled by grain-boundary diffusion.

4. Conclusions

Transmission electron microscopy and electron diffraction have revealed the formation of modulated structures and associated satellites in supersaturated Co–3% Ti–X (X = La, Fe, Nb) alloys on precipitation. The microstructural changes strongly suggest a spinodal mode of decomposition in these alloys in the range 823–973 K. Addition of niobium to the binary alloy increased the critical temperature for coherent spinodal decomposition, T_s^*, whereas iron addition has shown the reverse effect.

The addition of 0.1% La to Co–3% Ti alloy did not lead to a significant change in hardness from that of the binary alloy, either in solution-treated or aged conditions. In the case of Co–3% Ti–2% Nb, considerable extra strengthening was observed and could be related to the difference in the lattice parameters of the coexisting phases. The addition of iron to the binary alloy reflects that iron replaces the cobalt, whereas niobium and lanthanum replace titanium. This contributes to the solid solution and precipitation hardening.

All the binary and ternary alloys show discontinuous precipitation. The process is slow; its occurrence and rates are extremely structure sensitive and a competition exists everywhere between incoherent discontinuous precipitation and advanced coherent general precipitation. It is therefore inferred that the reactants and products for the discontinuous precipitation forces are each close to equilibrium and that the growth of the discontinuous product is determined primarily by the difference between coherent and incoherent equilibria. Analysis of the experimental (maximum) rate and spacing data on the basis of volume gives a reasonable accord that the addition of niobium raises and iron addition lowers the limiting temperature and kinetics of discontinuous precipitation in the alloy.

The kinetics of coarsening of the modulations (Stage I) obeys $\lambda^3 - \lambda_0^3 = kt$ relationship. The microstructure evolves further by an additional stage of coarsening corresponding to a breakdown of the modulations, and eventually loss of coherency at the interface. In addition, discontinuous coarsening with a lamellar morphology occurred during the later stages of coarsening. The interfacial energy of Co_3Ti particles in the matrix of the Co–3% Ti alloy at 873 K was found to be 9 mJ m^{-2}.

References

1. E. DIDERRICH, J. M. DRAPIER, D. COUTSRDIS and L. HABRAKEN, *Cobalt* **1** (1975) 7.
2. D. M. DAVIES and B. RALPH, *J. Microscopy* **96** (1972) 987.
3. A. J. ARDELL and R. B. NICHOLSON, *Acta Metall.* **14** (1966) 1295.
4. R. W. FOUNTAIN and W. D. FORGENG, *Trans. TMS-AIME* **215** (1959) 998.
5. R. W. FOUNTAIN, G. M. FAULRING and W. D. FORGENG, *ibid.* **221** (1961) 747.
6. H. BIBRING and J. MANENC, *Compt. Rend. Acad. Sci. Paris* **249** (1959) 1508.
7. YE. K. ZAKHAROV and B. G. LIFSCHITZ, English Abstracts of Selected Articles from Soviet Block and Mainland China Technical Journals, Series IIIm (1960).
8. A. L. BEREZINA and K. V. CHUISTOV, *Phy. Met. Metallogr.* **22**(3) (1966) 84.
9. *Idem., ibid.* **27**(2) (1969) 189.
10. O. YE. TKACHENKO and K. V. CHUISTOV, *ibid.* **29**(4) (1972) 159.
11. M. I. ZAKHAROVA and N. A. VASIL'YEVA, *ibid.* **33**(5) (1972) 119.
12. M. N. THOMPSON, PhD thesis, University of Cambridge, UK (1971).
13. M. N. THOMPSON and J. W. EDINGTON, "Microscopie Electronique", Vol. 2 (Favart, Paris, 1970) p. 545.
14. *Idem.*, in "Second International Conference on the strength of Metals and Alloys", Asilomar, CA (1971) p. 1150.
15. J. M. BLAISE, P. VIATOUR and J. M. DRAPIER, *Cobalt* **49** (1970) 192.
16. B. J. PIEARCEY, R. JACKSON and B. B. ARGENT *J. Inst. Met.* **91** (1962) 257.
17. D. E. LAUGHLIN and J. W. CAHN, *Acta Metall.* **23** (1975) 329.
18. P. E. J. FLEWITT, *ibid.* **22** (1974) 47.
19. J. SINGH, C. M. WAYMAN, J. MAZUMDER, S. RANGANATHAN and S. LELE, *Met. Trans.* **A19** (1988) 1703.
20. H. KUBO and C. M. WAYMAN, *ibid.* **A10** (1979) 633.
21. F. H. WOHLBIER (Ed.), "Diffusion and Defect Data", Vol. 13 (*Trans. Tech. Publ.*, Aedermannsdorf, Switzerland, 1976) p. 34.
22. I. M. LIFSHITZ and V. V. SLYOZOV, J. Phys. Chem. Solids **19** (1961) 35.
23. C. WAGNER, *Z. Electrochem.* **65** (1961) 581.
24. A. J. ARDELL, *Met. Trans.* **1** (1970) 525.
25. W. B. PEARSON, "The Crystal Chemistry and Physics of Metals and Alloys" (Wiley Interscience, New York, 1972). p. 151.

26. B. G. LEFEVRE, A. T. D'ANNESSIA and D. KALISH, *Met. Trans.* **A9** (1978) 577.
27. L. H. SCHWARTS and J. T. PLEWES, *Acta Metall.* **22** (1974) 911.
28. J. W. CAHN, *ibid.* **14** (1966) 477.
29. W. GUST, B. PREDEL and TAT. T. NGUYEN, *Z. Metallkde* **67** (1976) 10.
30. J. W. CHAN, *Acta Metall.* **11** (1963) 1275.
31. N. F. MOTT and F. R. N. NABARRO, *Proc. Phys. Soc.* **52** (1940) 86.
32. E. OROWAN, in "Symposium on Internal Stresses in Metals and Alloys" (Institute of Metals, London, 1948) p. 451.
33. R. J. LIVAK and G. THOMAS, *Acta Metall.* **19** (1971) 497.
34. S. D. DAHLGREN, *Met. Trans.* **A8** (1977) 347.
35. R. I. SAUNDERSON, P. WILKES and G. M. LORIMER, *Acta Metall.* **26** (1978) 1357.
36. J. SINGH and G. R. PURDY, *J. Mater. Sci.* **22** (1987) 2918.
37. I. G. SOLORZANO and G. R. PURDY, *Met. Trans.* **A15** (1984) 1055.
38. D. A. PORTER and J. EDINGTON, *Proc. R. Soc.* **358A** (1977) 335.
39. A. PERVOIC and G. R. PURDY, *Acta Metall.* **29** (1982) 53.
40. M. HILLERT, *Met. Trans.* **3** (1972) 2729.
41. K. N. TU and D. TURNBULL, *Acta Metall.* **15** (1967) 369.
42. R. A. FOURNELLE and J. B. CLARK, *Met. Trans.* **3** (1972) 2757.
43. N. LANGE and G. R. PURDY, "Report of Royal Institute Technology", Stockholm (1967).
44. D. B. WILLIAMS and E. P. BUTLER, *Int. Met. Rev.* **26** (1981) 153.
45. C. ZENER, *Trans. AIME* **167** (1946) 550.
46. H. I. AARONSON and J. B. CLARK, *Acta Metall.* **16** (1968) 845.
47. D. TURNBULL, *ibid.* **3** (1955) 55.
48. Y. C. LIU and H. I. AARONSON, *ibid.* **16** (1968) 1343.
49. M. KORCHYNSKY and R. W. FOUNTAIN, *Trans. Met. Soc. AIME* **215** (1959) 1033.
50. H. TSUKAKINO and R. NOZATO, *J. Mater. Sci.* **19** (1984) 3013.
51. J. SINGH, S. LELE and S. RANGANATHAN, *J. Mater. Sci.* **15** (1980) 2010.

Received 3 *June*
and accepted 14 *June* 1991